THE FLORIDA STATE UNIVERSITY

COLLEGE OF ARTS AND SCIENCES

AN IDEALIZED MODEL OF UPWELLING OFF PERU

by

Ruth Preller
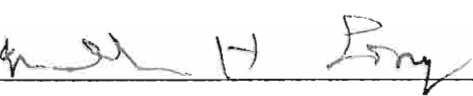
A thesis submitted to the
Department of Meteorology
in partial fulfillment of the
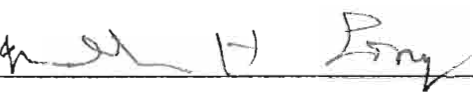requirements for the degree of
Master of Science.

Approved:

_____
Professor Directing Research

_____

_____

_____

_____

December, 1978

ABSTRACT

The x-y-t, two layer, β-plane numerical model developed by

Hurlburt (1974) is used to examine the upwelling system off Peru. The

region off Peru from 14°S to 15°30'S is one of strong and persistent

upwelling. The most distinctive feature of the Peruvian upwelling cir-

culation is a predominant poleward flow. The Hurlburt model, when

forced by wind stress only, shows no poleward flow. When additional

forcing, due to the effect of the atmospheric pressure gradient, is

applied in the model a dominating poleward flow results. In time, the

effects of wind stress are felt on the upper layer and an equatorward

flow develops near the coast. Two functional representations of the

actual topography are used in the model and compared to a flat bottom

case. Results show that the observed upwelling maximum approximately

40 km north of 15°S is due to the effects of a broad flatish shelf.

The upwelling maximum south of 15°S is the result of a mesoscale topog-

raphic feature, a seamount. Variations of meridional and zonal flow in

cases with E-W sloping topography are explained in terms of conserva-

tion of potential vorticity and conservation of mass transport over the

seamount. Based on Ekman dynamics, vertical cross sections of the

model results show strong poleward flows with a narrow layer of equa-

torward flow near the coast. As a result of the effects of rotation

model results show strong poleward flows with a narrow layer of equa-

torward flow near the coast. As a result of the effects of rotation

on this poleward flow, the vertical cross sections reveal offshore flow

in the upper 40 m and in a narrow layer over the shelf, with a thicker
onshore layer between the two. These circulation patterns agree closely
with observation.

ACKNOWLEDGMENTS

special friends Jeff Hawkins and David Adamec without whose under-
standing and caring this thesis might have been completed.

TABLE OF CONTENTS

LIST OF FIGURES

LIST OF TABLES

x

1. INTRODUCTION

The need to study coastal upwelling from an ecological and climatic standpoint has been well-known to scientists from many disciplines. From the viewpoint of the physical oceanographer, coastal upwelling is an important feature in the study of eastern ocean circulation. Various field programs, CUE I and II off the coast of Oregon and JOINT I off the coast of Northwest Africa, both part of the Coastal Upwelling Ecosystems Analysis Program (CUEA), have examined the upwelling system in these regions. More recently, during 1976-1977, the field experiment, JOINT II, has focused on upwelling off the coast of Peru. Peru is the richest of all the world's upwelling areas. This is due to the fact that upwelling does not migrate up the coast as in other upwelling regions. Thus the Peruvian coast is dominated by strong and persistent upwelling. It is the upwelling circulation of this region that will serve as the topic of the present study.

Many investigators have realized the usefulness of numerical models in understanding the dynamics of coastal upwelling. The model of O'Brien and Hurlburt (1972) examined upwelling for the f-plane case. Hurlburt and Thompson (1973) extended the investigation to upwelling on a β-plane. In the numerical model of Hurlburt (1974), the effects of various types of coastline geometry and bottom topography were discussed. Peffley and O'Brien (1976) continued this line of study by invarious types of coastline geometry and bottom topography were discussed. Peffley and O'Brien (1976) continued this line of study by in-

1

corporating into the Hurlburt model the actual coastline and topography
of the Oregon coast.

The present study uses the Hurlburt model (1974) to investigate
upwelling off the coast of Peru. The upwelling circulation in this re-
gion appears uniquely different from that of Oregon and Northwest
Africa. Smith (1978a) states "The response of the currents in the re-
gion off Northwest Africa and Oregon is closely coupled to the local
wind -- but not so off Peru where distantly caused phenomenon may dom-
inate local effects." Brink et al., (1978) have observed that
though the wind stress in this region is to the northwest, the mean
flow is generally towards the southeast. This flow was previously ob-
served by Smith et al., (1971). Smith (1978b) suggests that fluctua-
tions in the current propagating in the poleward direction may be baro-
clinic Kelvin waves, originating equatorward of 10°S and propagating
past 15°S. The fact that fluctuations are not well correlated with the
local winds suggests that a simply wind driven system is not sufficient
to explain the currents observed off Peru. The Hurlburt numerical
model, driven only by wind stress also does not simulate the flows ob-
served off Peru. The question to be answered then is: What is the
forcing mechanism needed to be incorporated into the model to obtain
the observed poleward flow over the shelf?

Various theories have been proposed to explain the cause of a
poleward flowing undercurrent. Garvine (1971) has shown the dynamic
importance of the longshore pressure gradient to a steady state upwell-
ing model. He provides, however, no physical mechanism for the produc-
tion of this longshore pressure gradient. He does suggest that "wind
ing model. He provides, however, no physical mechanism for the produc-
tion of this longshore pressure gradient. He does suggest that "wind
'piles up' the water in the direction of the wind stress". Hurlburt

and Thompson (1973) have shown that the β effect serves as a mechanism to induce a N-S sea surface slope. This, in turn, reduces the barotropic mode, allowing the formation of a lower layer poleward flow. In the present model, however, the β effect does not appear strong enough to induce the observed poleward flows.

Another possible mechanism has been suggested by Mittelstaedt (1978). In studying upwelling off the coast of Northwest Africa, Mittelstaedt suggests that the large scale atmospheric pressure gradient contributes "appreciably" to the longshore pressure variation in the ocean. The undercurrent may be a result of an imbalance between the local wind stress and large scale meridional pressure gradient. This is the mechanism chosen to be investigated in this paper.

The present study is the first attempt, using the Hurlburt model, to study the combined effects of atmospheric pressure gradient forcing and wind stress forcing on upwelling circulation. A longshore varying bottom topography will also be incorporated into this model. This topography will be an idealized, functional representation of the actual topography. The region of coastal Peru between Pisco (14°S) and San Juan (15°20'S) was purposely chosen by the JOINT II investigators as a region of strongest and most persistent upwelling. By using an idealized topography, representing the major large scale and mesoscale features in this region, the effects of these features on the upwelling circulation may best be determined.

Several cases will be examined in order to study the onset of coastal upwelling in a model with a Peru-like topography which is forced by both wind stress and atmospheric pressure gradient. Two coastal upwelling in a model with a Peru-like topography which is forced by both wind stress and atmospheric pressure gradient. Two specific regions along the Peru coast are found favorable to upwelling.

The location of these maximum upwelling regions are determined to be the result of topographic variations. A poleward flow is found in both upper and lower layers as a result of including atmospheric pressure gradient forcing in the model. Variations in the strength of this flow are affected by topography and latitude. Vertical cross shelf sections based on Ekman dynamics, reveal an onshore flow at mid-depths with an offshore flow in the upper layer and near the bottom on the shelf. Similar flows have been observed in the Peru upwelling region.

2. THE MODEL

The model, developed by Hurlburt (1974), is an x-y-t, two layer, primitive equation model on a β-plane. Driving forces for the model are both the wind and the atmospheric pressure gradient. The latter is new for upwelling models. The system of equations defining the model is nonlinear and the model retains the free surface.

A three dimensional view of the model geometry is shown in Fig. 1. The Peruvian coast, in the area of concern, is oriented at approximately a 45° angle in reference to latitude and longitude. The model coordinate system, corresponding to this orientation, has also been rotated 45°. This rotation results in a simple and economic way to obtain high resolution along the entire coast. A right-handed Cartesian coordinate system is used. The origin is determined by the intersection of the eastern most edge of the fluid, at a specific latitude, and a bottom reference level usually located at the greatest depth of the fluid.

The horizontal dimensions of the fluid are L_x and L_y. Both the eastern and western boundaries are straight solid walls while the northern and southern boundaries are open. These open ended boundary conditions allow the development of a Sverdrup interior in a basin of only mesoscale N-S extent. The retention of a Sverdrup interior is of dynamic importance to the upwelling system. The large-scale wind stress curl is small over the eastern side of oceans. The Sverdrup dynamic importance to the upwelling system. The large-scale wind stress curl is small over the eastern side of oceans. The Sverdrup

5
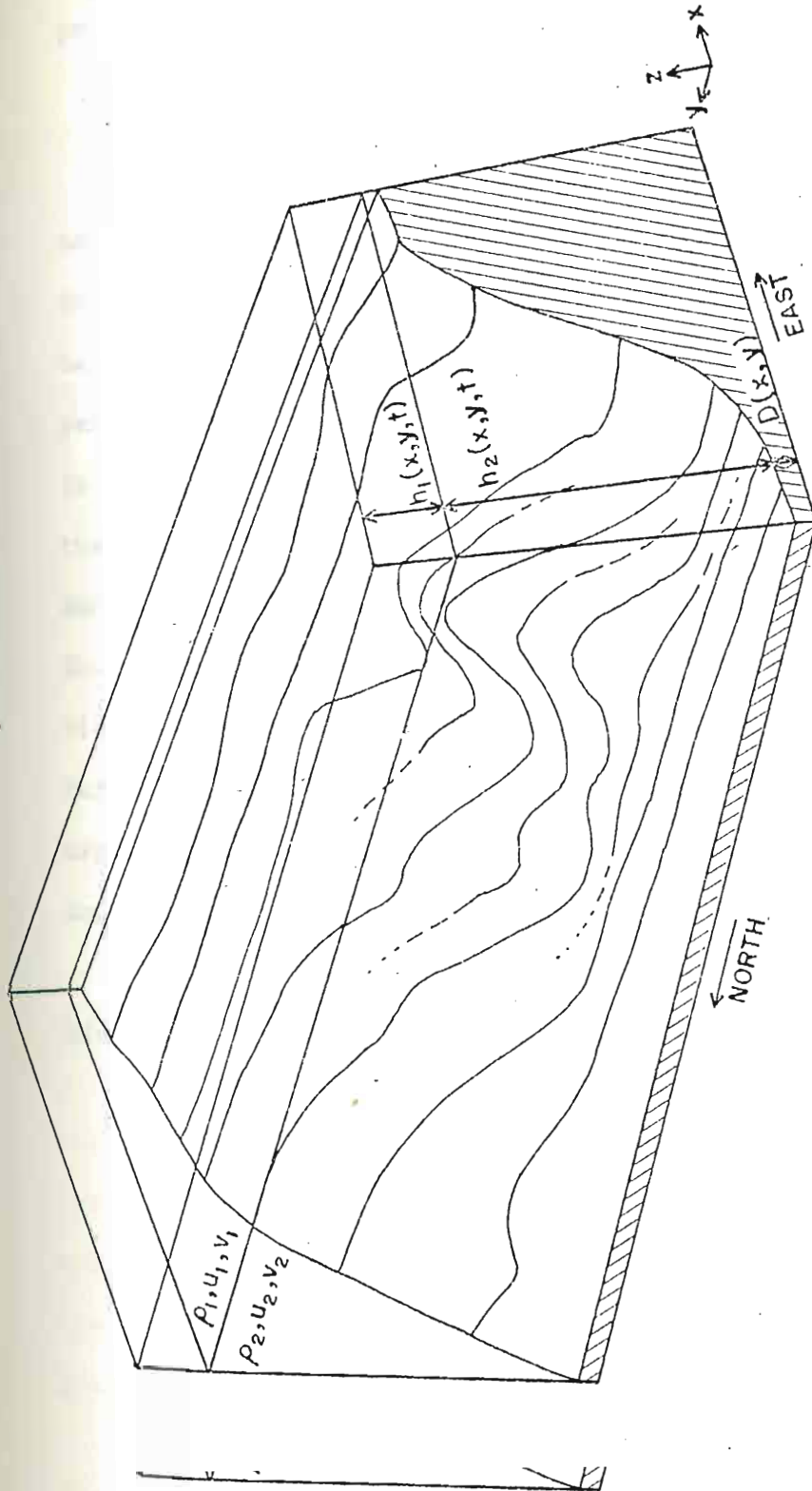
Fig. 1. Model geometry. The layer thicknesses h_1 and h_2 are dependent upon x,y, and t. D(x,y) is the height of the bottom above some reference level. The free surface and layer interface are shown here as flat surfaces for clarity. The interface is not allowed to intersect the topography. The coast is depicted as a straight line.

balance minimizes the strength of the wind-driven barotropic mode and permits a more realistic dominance of the baroclinic mode.

a. *The System of Equations*

The fluid used is assumed hydrostatic and Boussinesq. Thermodynamics, as well as thermohaline and tidal effects are neglected. Thompson (1974) has shown the importance of thermodynamics and thermohaline mixing when the interface between layers experiences large departures from its initial position. When the interfacial displacement is small, the exclusion of thermodynamics and thermohaline effects from the model does not prove a significant problem. In this model, as in Hurlburt (1974), the interface surfaces in approximately six days. Thus, without including thermodynamic and thermohaline effects, solutions beyond day five may not be useful and are not included here. Peffley and O'Brien (1976), however, have shown that five days of integration are long enough to understand the effect of topography on local circulation.

The model equations are the vertically integrated primitive equations on a β-plane for a stably stratified, rotating ocean:

$$\frac{\partial V_1}{\partial t} + \hat{V}_1 \cdot \nabla \hat{V}_1 + \hat{k} \times f\hat{V}_1 = -\frac{1}{\rho_1} \nabla P_a - g\nabla(h_1 + h_2 + D)$$

$$+ \frac{\hat{\tau}_s - \hat{\tau}_I}{\rho_1 h_1} + A\nabla^2 \hat{V}_1 \tag{1}$$

$$\frac{\partial h_1}{\partial t} + \nabla \cdot (h_1 \hat{V}_1) = 0 \tag{2}$$

$$\frac{\partial h_1}{\partial t} + \nabla \cdot (h_1 \hat{V}_1) = 0 \tag{2}$$

$$\frac{\partial \hat{V}_2}{\partial t} + \hat{V}_2 \cdot \nabla \hat{V}_2 + k \times f\hat{V}_2 = -\frac{1}{\rho_2} \hat{P}_a - g\nabla(h_1 + h_2 + D)$$

$$+ g'\nabla h_1 + \frac{\hat{\tau}_I - \hat{\tau}_B}{\rho_2 h_2} + A\nabla^2 \hat{V}_2 \qquad (3)$$

$$\frac{\partial h_2}{\partial t} + \nabla \cdot (h_2 \hat{V}_2) = 0 \qquad (4)$$

where the subscripts 1 and 2 denote upper and lower layers, respectively. Other terms are defined:

$$\hat{V} = u_i \hat{i} + v_i \hat{j}$$

$$f(x,y) = f_o + \beta(y - y_o) + \beta(x - x_o)$$

$$g' = g(\rho_2 - \rho_1)/\rho_2$$

$$\hat{\tau}_s = \tau_{sx} \hat{i} + \tau_{sy} \hat{j} \qquad (5)$$

$$\hat{\tau}_I = \rho C_I |\hat{V}_1 - \hat{V}_2|(\hat{V}_1 - \hat{V}_2)$$

$$\hat{\tau}_B = \rho C_B |\hat{V}_2| \hat{V}_2$$

where i = 1, 2 denotes layers.

The boundary conditions used in the model are no slip and kinematic for the eastern and western boundaries. A quasi-symmetric boundary condition, after Hurlburt and Thompson (1973), is used for the northern and southern boundaries. The boundary condition sets longshore derivatives equal to zero in Eqs. (1) - (4), except for the N-S pressure gradient, atmospheric pressure gradient and in the continuity equation.

Two major assumptions are required to determine the N-S pressure gradient, atmospheric pressure gradient and in the continuity equation.

Two major assumptions are required to determine the N-S pressure gradient. First the v field must be in nearly geostrophic balance such that:

$$fv_1 = g \frac{\partial}{\partial x} (h_1 + h_2 + D)$$

$$fv_2 = g \frac{\partial}{\partial x} (h_1 + h_2 + D) - g' \frac{\partial h_1}{\partial x}$$

Taking $\frac{\partial}{\partial y}$ of these equations and integrating over x, along with the fact that the N-S pressure gradient is set equal to zero at the western boundary and the atmospheric pressure gradient is constant across the basin, the equations are

$$g \frac{\partial}{\partial y} (h_1+h_2+D) \Big|_x = \int_{-L_x}^{x} \beta v_1' \, dx + \int_{-L_x}^{x} f \frac{\partial v_1'}{\partial y} \, dx \qquad (6)$$

$$[g \frac{\partial}{\partial y} (h_1+h_2+D) - g' \frac{\partial h_1}{\partial y}] \Big|_x = \int_{-L_x}^{x} \beta v_2' \, dx + \int_{-L_x}^{x} f \frac{\partial v_2'}{\partial y} \, dx \qquad (7)$$

$$+ [g \frac{\partial}{\partial y} (h_1+h_2+D) - g' \frac{\partial h_1}{\partial y}] \Big|_{-L_x}$$

Since the longshore derivatives of velocity are assumed small, with the exception of $\frac{\partial v}{\partial y}$ in the continuity equation, a second assumption

$$\Big| \int_{-L_x}^{x} f \frac{\partial v_i'}{\partial y} \Big| << \Big| \int_{-L_x}^{x} \beta v_i' \, dx \Big|.$$

further simplifies Eqs. (6) and (7).

The use of the actual velocities derived from the model in this boundary condition results in an unstable flow. Consistent with the geostrophic approximation, the ageostrophic part of the baroclinic velocity is subtracted from the model velocity in Eqs. (6) and (7) and the instability is removed. Thus the terms, v_1' and v_2', which appear in the above equations are model velocity minus the ageostrophic part of the instability is removed. Thus the terms, v_1' and v_2', which appear in the above equations are model velocity minus the ageostrophic part of the baroclinic velocity. This quantity can be obtained by developing

a modal analysis of the two layer system. The baroclinic velocity is defined

$$\hat{V}_{BC} = \hat{V}_1 - \hat{V}_2 \tag{8}$$

with the condition for the purely baroclinic case

$$\hat{V}_1 h_1 + \hat{V}_2 h_2 = 0 \tag{8a}$$

The barotropic velocity is given by

$$\hat{V}_{BT} = \frac{\hat{V}_1 h_1 + \hat{V}_2 h_2}{h_1 + h_2} \tag{9}$$

with the condition for the purely barotropic case

$$\hat{V}_1 = \hat{V}_2 \tag{9a}$$

The total velocities are then written as a linear combination of the barotropic and baroclinic components

$$\hat{V}_1 = C_1 \hat{V}_{BC} + C_1' \hat{V}_{BT}$$

$$\hat{V}_2 = C_2 \hat{V}_{BC} + C_2' \hat{V}_{BT} \tag{10}$$

Thus, from this system of six equations, it may be seen that

$$C_1' = C_2' = 1 \tag{11a}$$

Solving for the baroclinic mode yields

$$C_1 = \frac{h_2}{h_1 + h_2}$$

$$\tag{11b}$$

$$C_2 = - \frac{h_1}{h_1 + h_2}$$

$$\tag{11b}$$

$$C_2 = - \frac{h_1}{h_1 + h_2}$$

Substituting the C values, the velocities in terms of the two modes are

$$\hat{V}_1 = \frac{h_2}{h_1+h_2} \hat{V}_{BC} + \hat{V}_{BT}$$

$$\hat{V}_2 + - \frac{h_1}{h_1+h_2} \hat{V}_{BC} + \hat{V}_{BT} \qquad (12)$$

Now the baroclinic velocities may be broken up into two parts, geostrophic and ageostrophic

$$\hat{V}_{BC} = \hat{V}_{BCg} + \hat{V}_{BCa} = \frac{g'}{f} \frac{\partial h_1}{\partial x} + \hat{V}_{BCa}$$

Applying this equation to Eq. (12), the ageostrophic part of the baroclinic velocity in layers 1 and 2 respectively are

$$\hat{V}_A = \frac{h_2}{h_1+h_2} \hat{V}_{BCa} = \hat{V}_1 - \hat{V}_{BT} - \frac{h_2}{h_1+h_2} \hat{V}_{BCg}$$

$$-\frac{h_1}{h_2} \hat{V}_A = -\frac{h_1}{h_1+h_2} \hat{V}_{BCa} = \hat{V}_2 - \hat{V}_{BT} + \frac{h_1}{h_1+h_2} \hat{V}_{BCg} \qquad (13)$$

Thus $\hat{V}_1'$ and $\hat{V}_2'$ of Eqs. (6) and (7), representing the barotropic part of the velocity and the geostrophic part of the baroclinic velocity may be written

$$\hat{V}_1 = \hat{V}_1 - \hat{V}_A$$

$$\hat{V}_2 = \hat{V}_2 + \frac{h_1}{h_2} \hat{V}_A \qquad (14)$$

Along with the boundary conditions, initial conditions are required. The model is started from rest. The wind stress and pressure gradient forcing are applied impulsively at initial time. Incorporation of these boundary and initial conditions closes the system. The gradient forcing are applied impulsively at initial time. Incorporation of these boundary and initial conditions closes the system. The complexities of such a nonlinear system require numerical methods to obtain a solution.

b. *Numerical Formulation*

The finite differencing scheme, incorporated into the model by O'Brien and Hurlburt (1972) and Hurlburt (1974), is semi-implicit in the x-direction and explicit in the y-direction. Use of a semi-implicit scheme in the x-direction allows a larger time step than that usually dictated by the Courant-Friedrichs-Lewy (CFL) linear stability condition. Use of an explicit scheme in the y-direction places the approximate restriction on the time step

$$\Delta t = (\Delta y \text{ min})/ [g (H_1 + H_2) \text{ max}]^{\frac{1}{2}} \qquad (15)$$

given by the CFL condition. From the economic standpoint, a limit must be placed on the basin depth and the fine resolution of longshore scales, in spite of the desire for high resolution, small y and a realistically deep basin.

Other properties of the finite differencing scheme are use of leapfrog time differencing for the Coriolis and nonlinear terms and use of the Crank-Nicholson (1947) scheme, which treats the diffusive terms semi-implicitly in the x-direction. Other frictional terms are lagged in time. Advective terms are handled by quadratic averaging (Scheme F) from Grammeltvedt (1969).

Reduction of the number of necessary grid points is accomplished by using a variable resolution grid. The Δx used in the model is a discrete function of x. In the eastern most 40 km, the value of Δx is 2 km. Moving westward, Δx takes on the values; 4, 10, 40 and 100 km. In the y-direction, an analytically stretched variable was used. This

In the y-direction, an analytically stretched variable was used. This stretched variable is defined by Shulman (1970) as

$$S(a) = C \left[\alpha a + \sum_{k=1}^{N} \tanh \left[\frac{a-a_k}{\gamma k} \right] + b \right] \qquad (16)$$

where

$$S(0) = 0, \quad S(1) = 1$$

and

$$a = y/L_y$$

If q, any dependent variable, is defined

$$q = q(S(a(y)))$$

then the first and second derivatives of q are

$$\frac{\partial q}{\partial y} = \frac{1}{L_y} \frac{dS}{da} \frac{\partial q}{\partial S}$$

$$\frac{\partial^2 q}{\partial y^2} = \frac{1}{L_y^2} \left(\frac{ds}{da} \right)^2 \frac{\partial^2 q}{\partial S^2} + \frac{1}{L_y^2} \frac{d^2 S}{da^2} \left[\frac{\partial q}{\partial S} \right]^2$$

In the model

$$N = 1, \quad a_k = .5, \quad \gamma = .2, \quad \alpha = 2.$$

Implementation of this stretched coordinate approach gives a y grid resolution of minimum Δy = 4.1 km in the center of the basin and maximum Δy = 13.1 km at the northern and southern boundaries.

Hurlburt and Thompson (1973) have shown that the longshore flow and upwelling circulation are independent of basin width, if the basin is wide enough to separate the eastern and western boundary circulations. In order that longshore flows are independent of basin width, a Sverdrup interior must be created. They have shown that the width re-tions. In order that longshore flows are independent of basin width, a Sverdrup interior must be created. They have shown that the width required is greater than 1000 km for the value of β used in this model. The width of the present model is 1500 km so that western boundary cir-

culations have no effect on the eastern boundary and longshore flows are independent of basin width. In the east-west direction, a $\Delta x < 5$ km is required to resolve the boundary layers. Thus a fine grid is used in the eastern portion of the basin and a coarse grid used in the western part of the basin where solutions are relatively unimportant to this study.

c. *Cross Shelf Physics*

One of the assumptions used in the model is that Ekman dynamics is important to the vertical structure of the flow field. Ekman-like boundary layers are expected and observed near the surface, pycnocline and bottom, all regions of large vertical shear. It will be of interest then, to look at a vertical cross shelf section of the flow generated by the model. This cross sectional analysis is done using a method developed by Thompson (1974) in which analytical solutions are obtained for the departures from the vertical mean of the velocity fields. Boundary layers are thus introduced near the internal and external fluid interfaces. The simple upwelling circulation obtained from the vertically averaged equations is altered by the mass flux into and out of these boundary layers. If $\hat{V}'_j$ is the departure from the mean velocity within each layer, then the Ekman equations are

$$ k \times f \, \hat{V}'_j = A_v \frac{\partial^2 V_j}{\partial z^2} \qquad j = 1, 2 \qquad (17) $$

If the sea surface is designated by $z = 0$, the pycnocline by $z = b$, and the bottom by $z = c$, the statement of the problem becomes

$z = b$, and the bottom by $z = c$, the statement of the problem becomes

$$\frac{\partial^2 w_1}{\partial z^2} - s^2 w_1 = 0 \qquad\qquad b \le z \le 0$$

$$\frac{\partial^2 w_2}{\partial z^2} - s^2 w_2 = 0 \qquad\qquad c \le z \le 0 \qquad\qquad (18)$$

where

$$w_1 = u_1' + iv_1'$$

$$w_2 - u_2' + iv_2'$$

We also require the integral constraint that, when vertically integrated over the layer, w_j is zero. Four boundary conditions are used. At the surface, the perturbation velocity shear stress is equal to the wind stress. At the interface, the total flow is continuous and the perturbation shears are equal. The final boundary condition states that the total velocity at the bottom is zero. For a more detailed explanation of the method used, refer to Appendix 2.

The perturbation values are added to the mean flow to obtain the total velocity. Figures of the flow field obtained by this method for various sections along the coast will be shown in a later section. It should be understood that this Ekman flow is calculated as a device to demonstrate the vertical details of the flow. The results obtained are similar to observations off Peru.

d. *Bottom Topography*

The bottom topography used in this model is obtained from the O'Brien-Preller (1977) Peruvian nearshore bottom topography and coast-
The bottom topography used in this model is obtained from the O'Brien-Preller (1977) Peruvian nearshore bottom topography and coast-line map, Preller (1977), Fig. 2. Data used for this map were obtained during the 1977 CUEA JOINT II experiment off the coast of Peru. The
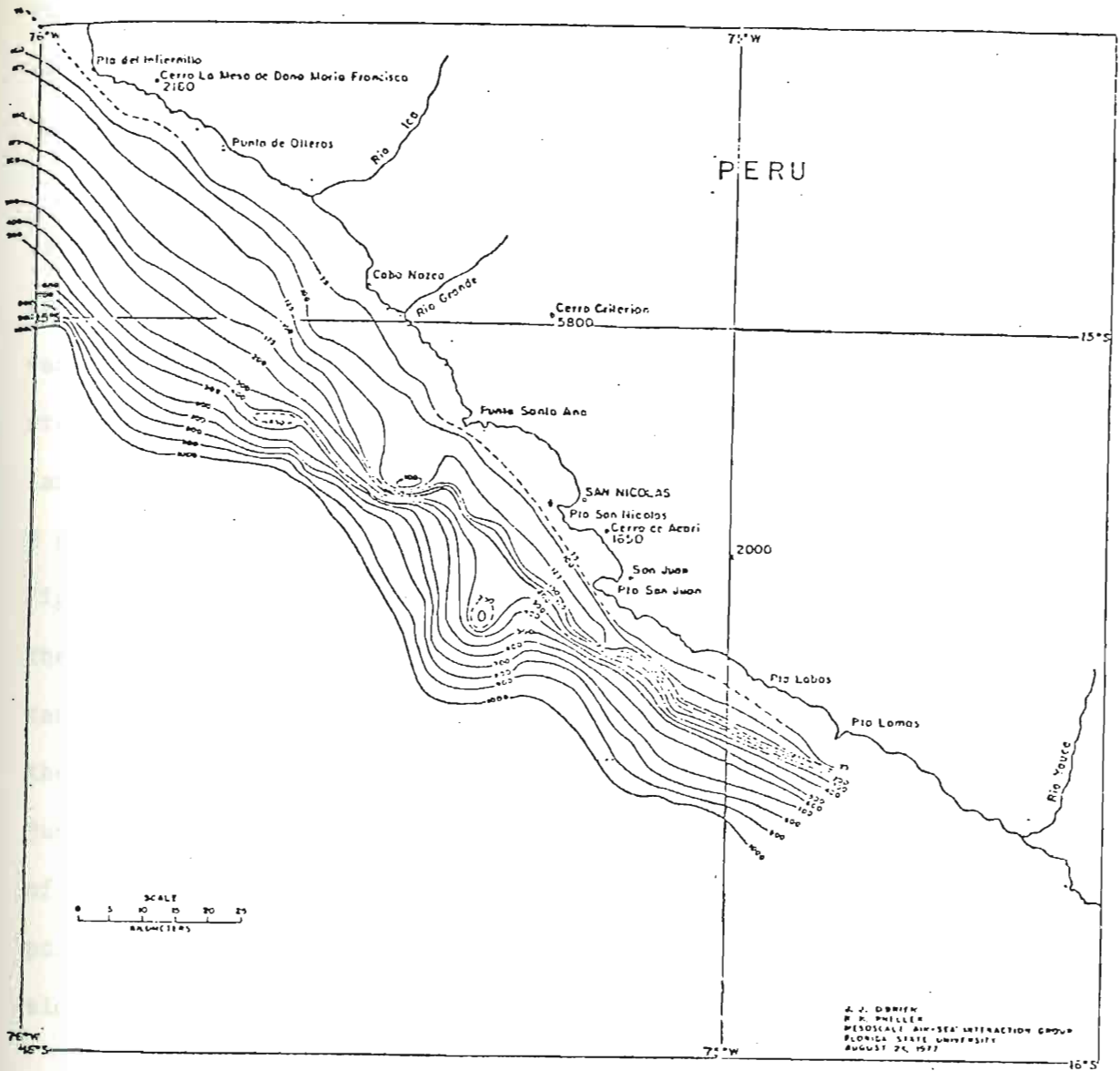
Fig. 2.   The O'Brien and Preller (1977) Peruvian bottom topography map.   Contour values are in meters.

coastline was taken from the No. 22012 map of the coasts of Peru and Chile by the Defense Mapping Agency Hydrographic Center. The data extend from approximately 14°13'S to 16°S in the N-S direction and 74°30'W to 76°W in the E-W direction.

Fig. 2 shows the Peruvian topography to be quite complex in the area of interest. Shelf widths range from approximately 20 km in the north to approximately 6 km in the south. The shelf slope itself is variable in the longshore direction as is the continental slope. The steepest shelf slopes occur south of Punta Santa Ana, in more particular, south of Punta San Juan. Observations of the coastline from Fig. 2 show it has a general orientation of 45° to latitude and longitude. Fig. 3 is an enlargement of Fig. 2, rotated at a 45° angle such that the coastline now is oriented in a N-S direction. In this figure, it can be seen that the continental slope begins to steepen just south of the intersection of 15°S and the coast. This steep slope continues to just south of Punta Santa Ana, where the slope flattens in the vicinity of Punta San Nicolas. Another major topographic feature seen at this point is a mesoscale seamount. South of the seamount, the continental slope again steepens.

The coastline also exhibits some prominent features as Cabo Nazca, Punta Santa Ana, Punta San Nicholas and Punta San Juan. Peffley and O'Brien (1976) however, have shown that coastline features are not as influential as topographic variations in determining the longshore upwelling circulation. In this simple model, the coastline is assumed to be straight and the model, as previously mentioned, is rotated 45° to welling circulation. In this simple model, the coastline is assumed to be straight and the model, as previously mentioned, is rotated 45° to latitude and longitude. Thus the model coastline is a straight line oriented in the N-S sense of the model.
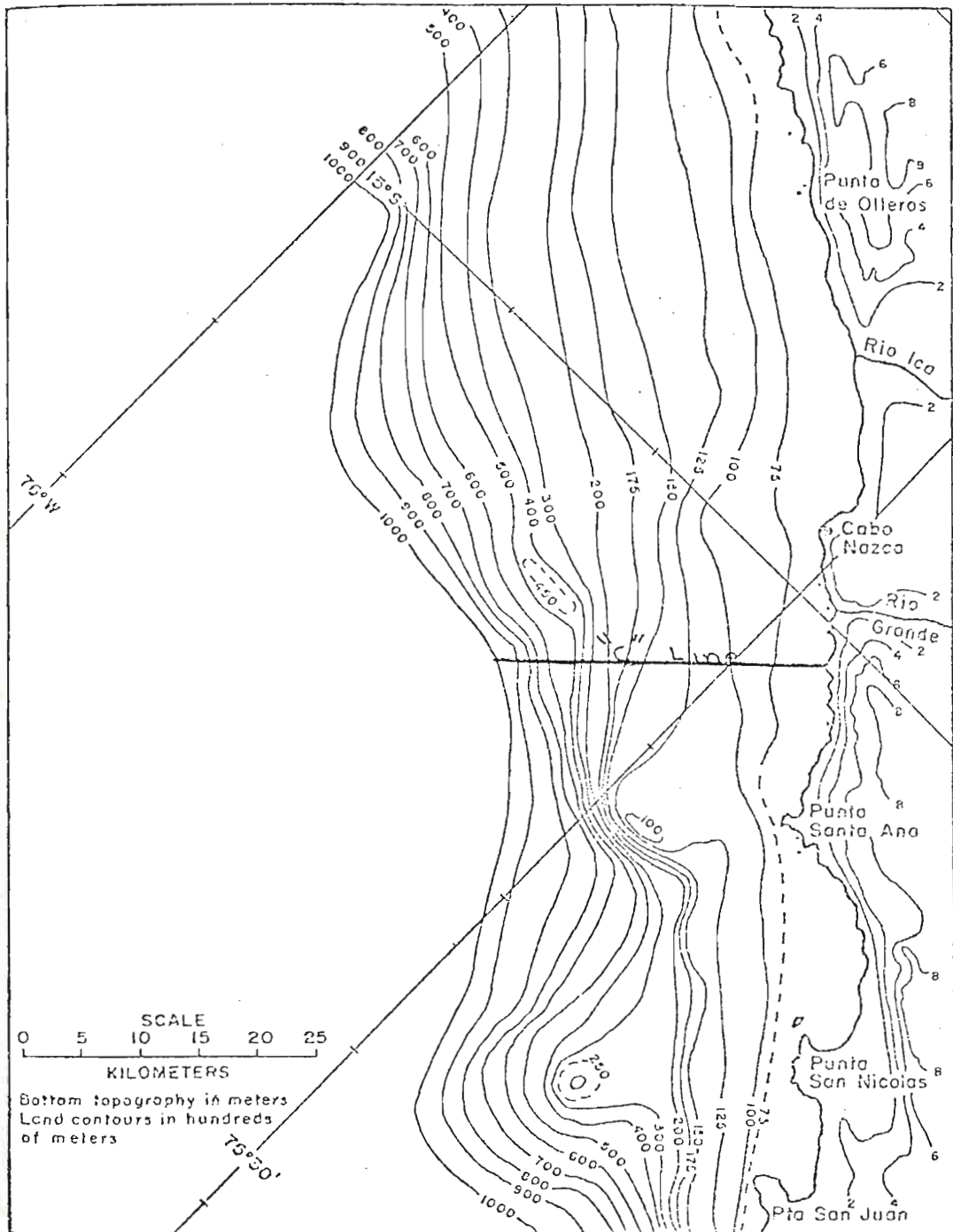
Fig. 3. A section of Fig. 2, rotated 45° counter-clockwise

Fig. 3. A section of Fig. 2, rotated 45° counter-clockwise
from North. Land contours have been added to the map of Fig. 2.
The "C" Line is a region from which large amounts of data were
gathered during JOINT II.

The topographies used in the cases examined here are functional estimates of the actual topography, representing the most distinctive topographic features. The first topography, shown in Fig. 4, exhibits two distinctive topographic features distinguishing the northern from the southern region of interest. The first is the broad flatish shelf and gently tilting continental slope in the north and the second, the steepening of both these slopes below 15°S.

The function used to obtain this idealized topography was a hyperbolic tangent function of the form

$$h(x,y) = c \left[\alpha x + \tanh \left(\frac{x - \gamma f(y)}{\sigma} \right) + b \right] \tag{19}$$

where f is also a hyperbolic tangent represented by

$$f(y) = k \left[\tanh \left(\frac{y + y'}{\sigma'} \right) + b' \right]$$

and

$$h(0,y) = 74000 = H$$

$$\lim_{x \to \infty} h(x,y) = 0$$

such that

$$b(y) = - \alpha f(y) = \tanh \left[\frac{(1-\gamma)f(y)}{\sigma} \right]$$

$$c(y) = \frac{H}{- \alpha f(y) - \tanh \left[\frac{(1-\gamma)f(y)}{\sigma} \right] + \tanh \left[\frac{-\gamma f(y)}{\sigma} \right]}$$

This hyperbolic tangent topography follows the actual topography closely. The maximum depth of 800 m is located 35 km from the coast in the north and 14 km in the south, corresponding to the actual topography. The functional estimate of the shelf extends to 15 km in the north and the north and 14 km in the south, corresponding to the actual topography. The functional estimate of the shelf extends to 15 km in the north and 5 km in the south, again a good representation of the real topography.
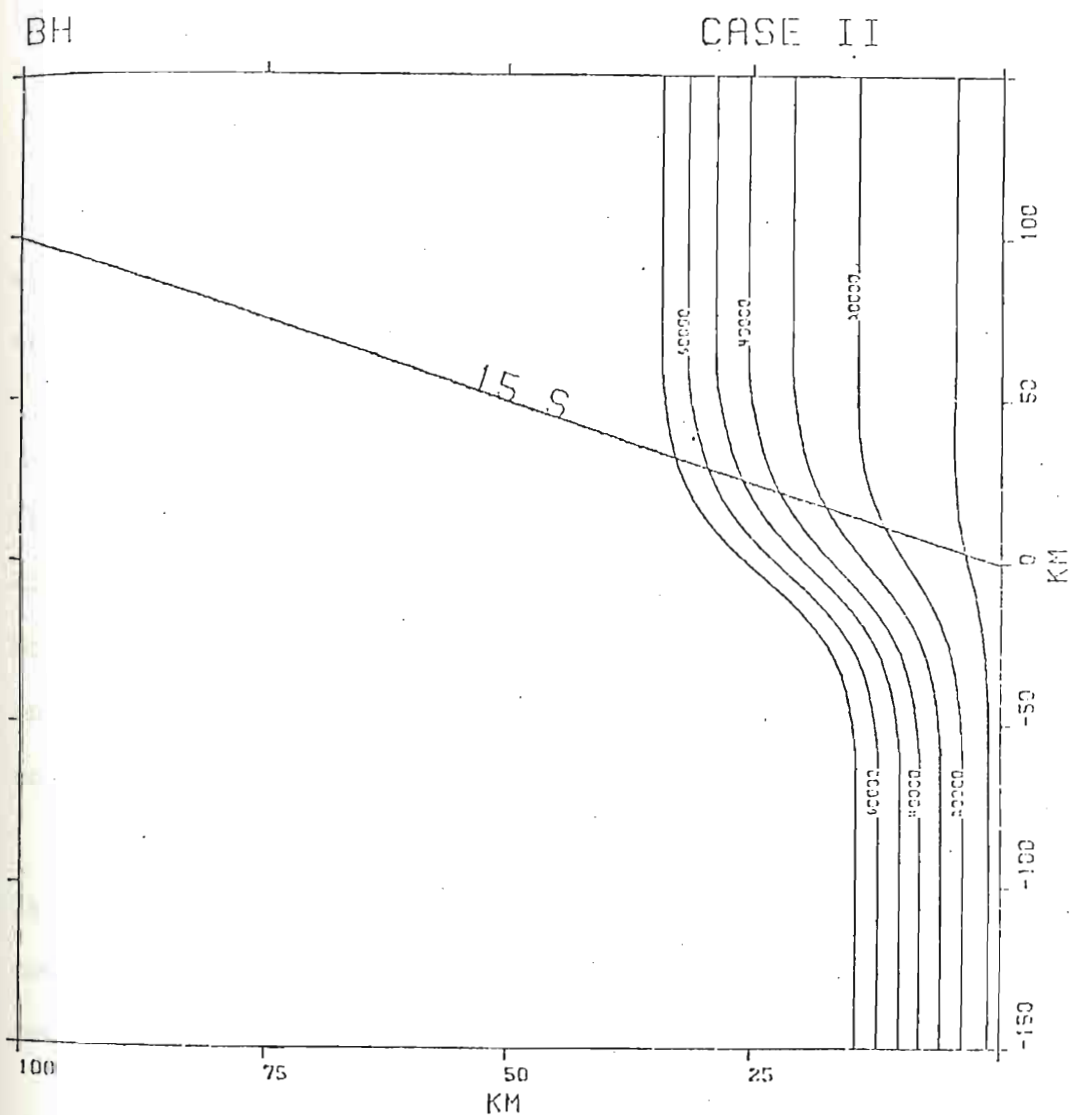
Fig. 4.   Case II topography.   A hyperbolic tangent, functional representation of the topography of Fig. 3.   The figure is rotated 45° counter-clockwise from North.   The right-hand side of the figure represents the coast and only the nearest 100 km to the coast is shown.   Zero, along the ordinate, indicates the intersection of 15° S with the coast.   The y extent of the figure is 300 km centered about 15° S.

The shelf and continental slope steepen in both Figs. 3 and 4 just south of the 15° south line. The hyperbolic tangent function proves to be a good representation of these two important features of the topography.

The second topography used is shown in Fig. 5. This case incorporates the mesoscale seamount into the previous idealized topography. The function used to estimate the seamount was an ellipse of the form

$$z = [\ c^2 - \frac{c^2}{a^2} (x-x_o)^2 - \frac{c^2}{b^2} (y-y_o)^2\ ]^{\frac{1}{2}} + z_o \qquad (20)$$

with z representing height above the reference level depth 800 m and the center of the seamount located at

$$x_o = 8 \text{ km} \qquad\qquad\qquad y_o = -41 \text{ km}$$

The ellipse was incorporated into the previous topography by using the ellipse value whenever it proved to be larger than the previous hyperbolic tangent value. A 1-2-1 smoother in the y-direction was applied once in order to join smoothly the two functions. Due to the fine resolution in x, smoothing is not required.

The functional representation of the seamount differs only slightly from the actual topography. The ellipse extends from 17 km to 67 km south of 15°S and 36 km offshore. The actual seamount extends from approximately 20 km to 60 km south of 15°S and 36 km offshore.

In both of the topographic representations described above, the values of the isobaths in the northernmost 50 km and southernmost 50 km of the basin are merely extensions of the isobath values at y = 100 km and y = -100 km respectively. These regions of y independent topography have been included to insure that derivatives in y be small near

22
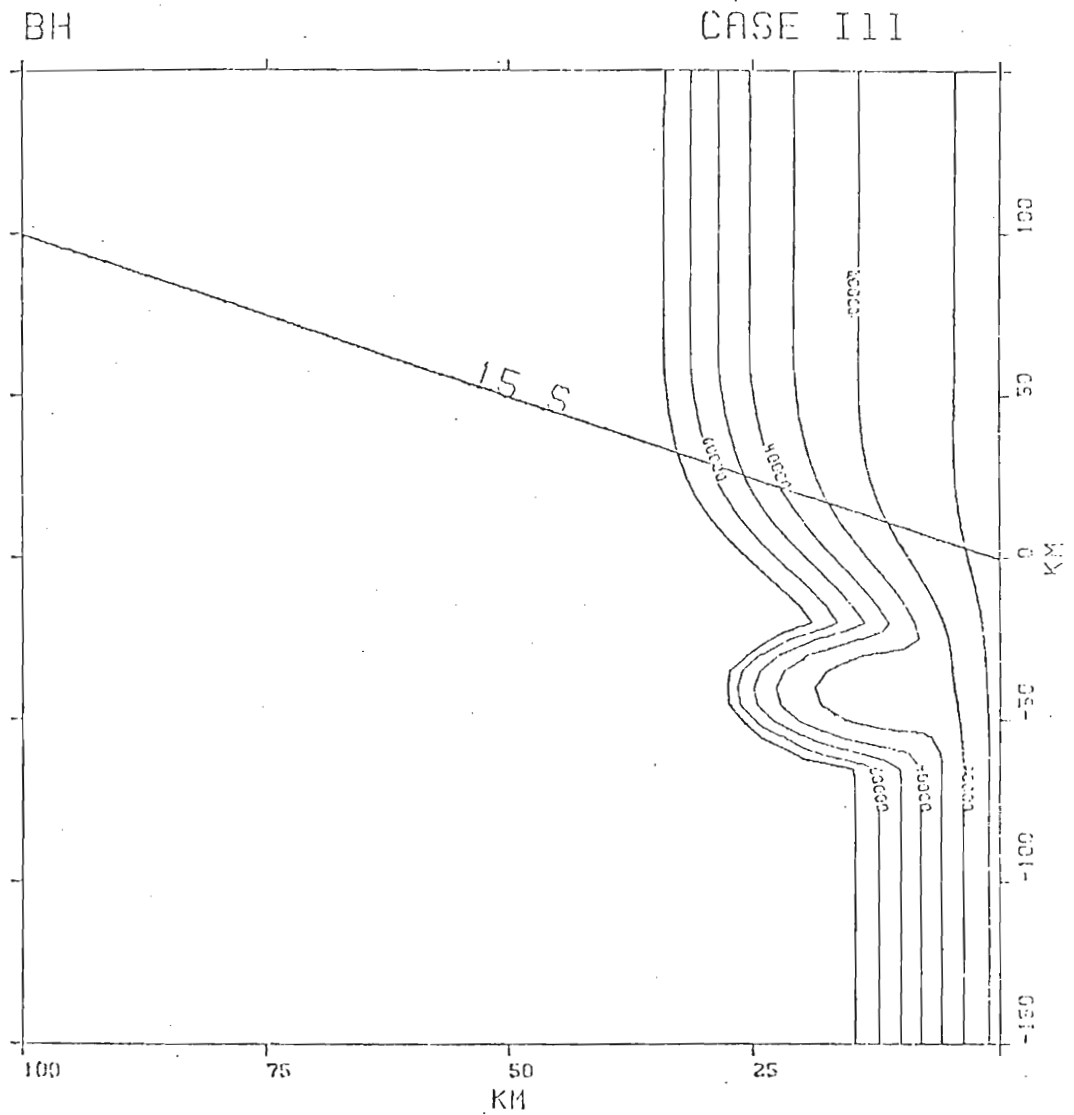
Fig. 5. Case III topography. An ellipse is added to the topography of Fig 4, as representative of the seamount. Most of the subsequent figures will have the 15 S latitude drawn, but unlabeled.

but unlabeled.

the boundaries, as required by the boundary condition.

The topography with and without the seamount has been used in the model as representative of the major features of the actual topography. Flat bottom model cases have also been used as a basis for this study.

3. CASE DESCRIPTIONS

A number of case studies incorporating the two idealized Peru bottom topographies and flat bottom were made. The parameter values given in Table 1 were common to all cases.

The dimensions of the basin were chosen on the basis of observations. The N-S extent of the basin, the area 150 km north and 150 km south of 15°S, contains the area of interest to the JOINT II experiments. There was a good deal of freedom in choosing the east-west extent of the basin. As stated previously, Hurlburt and Thompson have shown that if the basin is greater than 1000 km wide, the upwelling circulation in the model is not affected by the western boundary solution. For this model, the actual area of interest lies in the first 100 km from shore, so that basin width of 1500 km, not much larger than the minimum width, was chosen. The vertical extent of the basin was chosen to be 800 m. This is deeper than the expected maximum upwelling depth but was chosen to include flow over the continental slope and still retain an economical time step. Solutions using basins of this depth differ little, qualitatively, with basin depths of 0(200 m) as observed by Thompson (1974).

The permanent pycnocline is represented by the layer interface. Upwelling is then signified by the displacement of the interface from its initial position. The mean location of the pycnocline may be es-Upwelling is then signified by the displacement of the interface from its initial position. The mean location of the pycnocline may be estimated by observing the values for this area of Peru. Fig. 6, from

Table 1

Parameter	Symbol	Value
E-W basin extent	L_x	1500 km
N-S basin extent	L_y	300 km
Max basin depth	$(H_1+H_2)max$	800 m
Initial upper layer thickness	H_1	50 m
Initial lower layer thickness	H_2	variable
Coriolis parameter at y = 0 and 15°S latitude	f_o	$-.3764 \times 10^{-4} s^{-1}$
$\frac{\partial f}{\partial y}$, $\frac{\partial f}{\partial x}$	β	$1.56 \times 10^{-11} m^{-1} s^{-1}$
Horizontal eddy viscosity coefficient	A_H	$5 \times 10^{3} m^{2} s^{-1}$
Vertical eddy viscosity coefficient	A_v	$5 \times 10^{-3} m^{2} s^{-1}$
Upper layer density	ρ_1	$1.0 \times 10^{3} kg\ m^{-3}$
Lower layer density	ρ_2	$1.002 \times 10^{3} kg\ m^{-3}$
Gravitational acceleration	g	$9.8\ m\ s^{-2}$
Reduced gravity	g'	$2 \times 10^{-2}\ m\ s^{-2}$
Interfacial drag coefficient	C_I	1×10^{-5}
Bottom frictional drag coefficient	C_B	1×10^{-3}
Longshore pressure gradient	$\frac{\partial Pa}{\partial y}$	$1.25 \times 10^{-2} Nm^{-2}/m$
Time step	Δt	36 s
Grid increment in x direction	Δx	variable
Time step	Δt	36 s
Grid increment in x direction	Δx	variable
Grid increment in y direction	Δy	analytically stretched variable
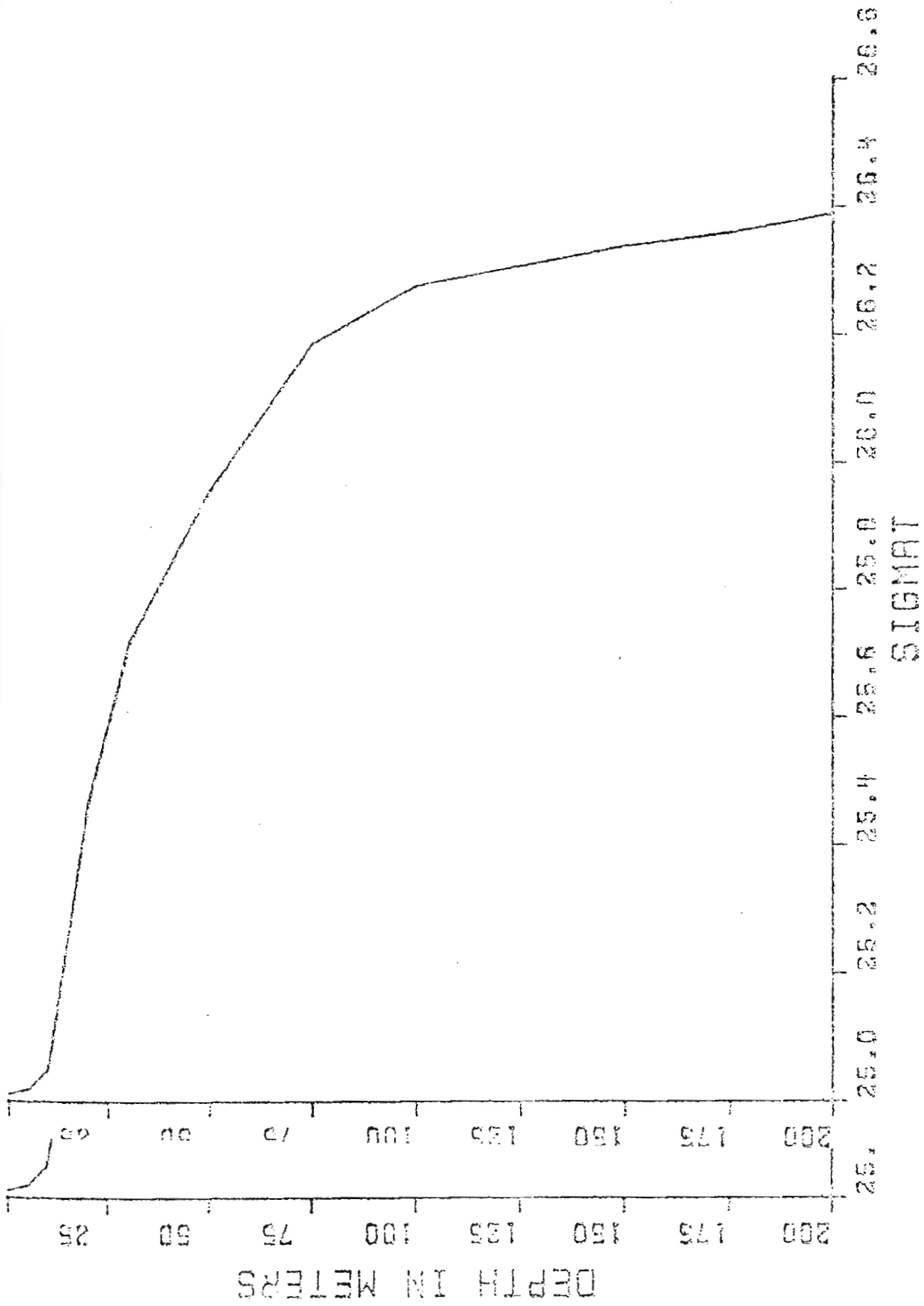
Fig. 6. Profile of the change of σ_t with respect to depth after Bart Barton (1978).

data obtained by Barton (1977), show the vertical variation of σ_t. The most dramatic changes occur from 20 m - 30 m so that a midpoint value of 50 m was chosen for the upper layer depth.

The horizontal eddy viscosity value was chosen to be $5 \times 10^3 \; m^2 s^{-1}$. This value may appear to be high when compared to the value of $10^2 \; m^2 \; s^{-1}$ used by Hurlburt (1974) and Hurlburt and Thompson (1973) or $5 \times 10^2 \; m^2 \; s^{-1}$, used by Peffley and O'Brien (1976). However, values as high as $2.1 \times 10^3 \; m^2 \; s^{-1}$ have been estimated by Stevenson et al. (1973) off of Oregon in 1972.

The value, $5 \times 10^{-3} \; m^2 \; s^{-1}$, for the vertical eddy viscosity, was chosen for simplicity of analysis, as a depth independent value. Allen (1973) also chose $A_v \simeq 5 \times 10^{-3} \; m^2 \; s^{-1}$, however larger values of $10^{-2} \; m^2 \; s^{-1}$ were used by Hsueh and O'Brien (1971). This smaller value was chosen on the basis of calculations of vertical eddy viscosity made by Tomczak (1970) based on data from the "Meteor" expedition in 1937. Actual values of vertical eddy viscosity, calculated from daily temperature variations on the N.W. Africa shelf, 10°N to 28°N, show an average value slightly below $10^{-2} \; m^2 \; s^{-1}$ for the first 30 m of water. According to Kullenburg (1971), the vertical eddy viscosity A_v is expected to decrease with depth. Incorporating this idea with the observed values obtained by Tomczak suggested $5 \times 10^{-3} \; m^2 \; s^{-1}$ for the value of A_v used in this model.

The difference between the upper and lower layer densities was chosen to be the commonly used value 2 kg m^{-3}. This value is slightly high as Smith (1978a) shows the waters off Peru to be somewhat less stratified with values of density difference being .8 kg m^{-3}.
high as Smith (1978a) shows the waters off Peru to be somewhat less stratified with values of density difference being .8 kg m^{-3}.

The value of the interfacial stress coefficient was chosen to be 10^{-5} after Thompson and O'Brien (1973). The bottom stress value of 10^{-3} was suggested by Proudman (1953). The value of Δt was chosen to be approximately 80% of the value dictated by the CFL condition.

The wind stress, shown in Fig. 7, is chosen to have zero curl in the upwelling region. The wind stress component, τ_{sy}, in the x-direction, was set equal to zero while τ_{sy} attains a maximum value of .05 Nm^{-2} in the upwelling region. This value is in agreement with observation by Smith (1978a).

The value of the pressure gradient term was chosen to agree with observation. When incorporated into the basic model case, this value was responsible for creating magnitudes of poleward flow similar to the observed values. An average pressure change taken from 1977 surface pressure maps is 7mb change over 10° of latitude. Using that value as an average, the pressure gradient over 300 km, the length of the basin, in mks units is 2.1 x 10^{-3} Nm^{-2}/m. The value used in the model, 1.25 x 10^{-2} Nm^{-2}/m, though somewhat high was chosen as the best parameterization of the actual flow. The atmospheric pressure gradient in the x direction was set equal to zero while the north-south pressure gradient remains a constant value through the basin.

Three cases will be discussed in this paper. All cases were started from rest and driven by the wind stress of Fig. 7, and the atmospheric pressure gradient. Case I is a flat bottom, straight coast case with a basin depth of 800 m and is referred to as the basic case. Case II, using the topography represented by Fig. 4, has a straight

Case II, using the topography represented by Fig. 4, has a straight coast and a maximum basin depth of 800 m. Case III, using the topography of Fig. 5, has a straight coast and 800 m basin depth. All cases
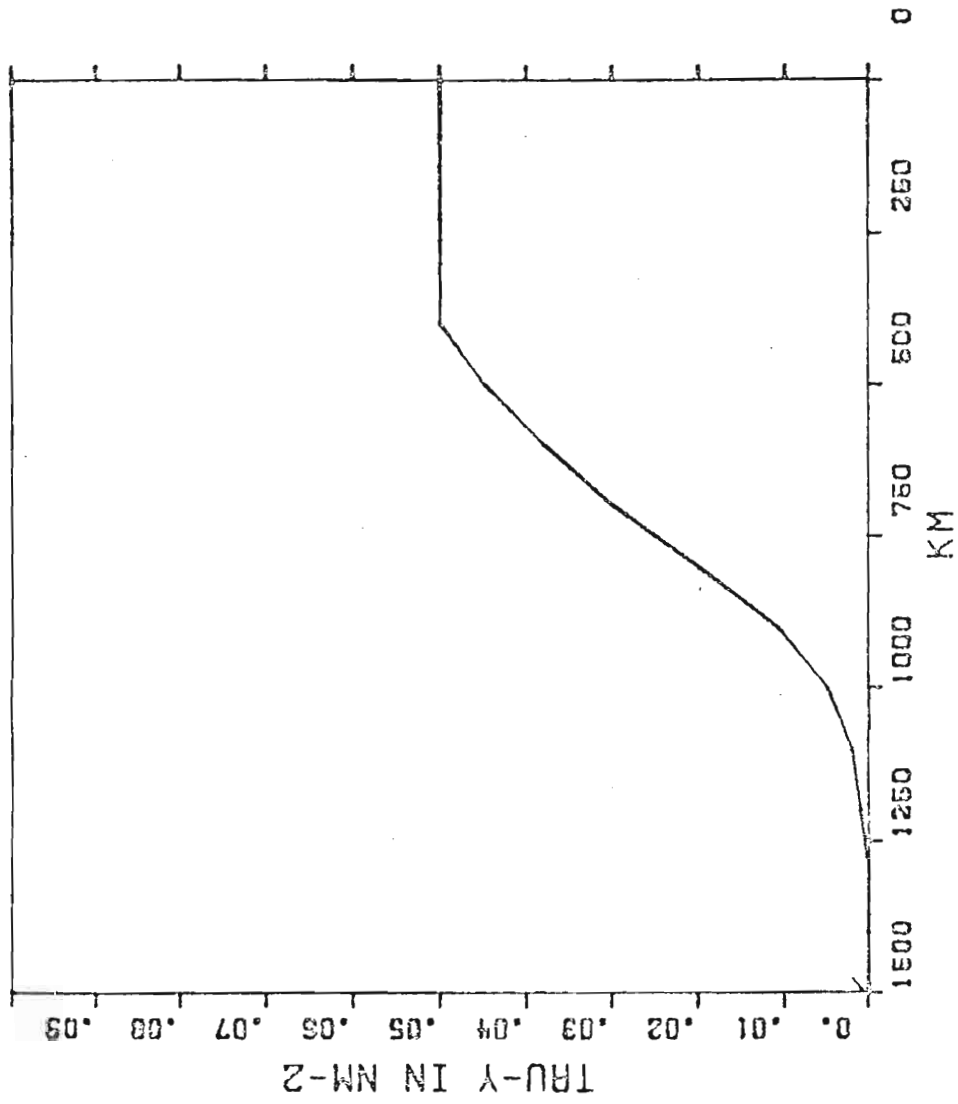
Fig. 7. An E-W profile of the y component of the wind stress used in all cases described in this paper. The x component was set equal to zero. The wind stress is y and time independent.

were integrated for five days with wind stress and pressure gradient values remaining unchanged.

4. RESULTS

Many case studies were made using the model described in Section 2. The results of these cases were observed by comparing five different fields determined by the model: the upper layer zonal velocity, upper layer meridional velocity, lower layer zonal velocity, lower layer meridional velocity, and pycnocline height anomaly. By observing the similarities and differences in the various cases, new insights into the dynamics of upwelling may be obtained.

a. *Dynamics*

The basic dynamics of upwelling on a β plane has been previously discussed by Hurlburt and Thompson (1973), however a short review will be beneficial to the understanding of this paper. For a flat bottom case with an equatorward wind stress, an equatorward surface jet and poleward undercurrent appear. The jet has been explained by a conservation of potential vorticity argument. The poleward flow is explained in terms of matching a near-zero Sverdrup interior to an upwelling boundary layer. In the upper layer, the offshore flow is weaker than the Ekman drift due to a N-S sea surface slope. In the region outside the upwelling zone, onshore flow in the lower layer is balanced geostrophically. Inside the upwelling region, geostrophy and Ekman drift break down to satisfy the boundary condition, u = 0, at the coast.

break down to satisfy the boundary condition, u = 0, at the coast.

31

Thus an equatorward acceleration appears in the upper layer and a pole-ward acceleration in the lower layer.

This study is particularly concerned with the development of the poleward undercurrent. This type of flow has been found when the long-shore pressure gradient reduces the barotropic mode near the coast. Hurlburt and Thompson (1973) have shown that a N-S sea surface slope may be induced by the β effect,

$$\int_{-L_x}^{x} \beta v_1 \, dx = g \frac{\partial}{\partial y} (h_1 + h_2 + D)\Big|_x - g \frac{\partial}{\partial y} (h_1 + h_2 + D)\Big|_{-L_x} \qquad (21)$$

In the present case, two important changes appear. First is the introduction of an atmospheric pressure gradient, $\frac{1}{\rho} \frac{\partial P_a}{\partial y}$. The effects of this term may be seen by looking at the linear y-momentum equations

$$\frac{\partial v_1}{\partial t} + f u_1 = -\frac{1}{\rho} \frac{\partial P_a}{\partial y} - g \frac{\partial}{\partial y} (h_1 + h_2 + D) + \frac{\tau_{sy}}{\rho_1 h_1} \qquad (22a)$$

$$\frac{\partial v_2}{\partial t} + f u_2 = -\frac{1}{\rho} \frac{\partial P_a}{\partial y} - g \frac{\partial}{\partial y} (h_1 + h_2 + D) + g' \frac{\partial h_1}{\partial y} - \frac{\tau_{By}}{\rho_2 h_2} \qquad (22b)$$

With the atmospheric pressure gradient positive, the entire term adds to the poleward flow. Due to the effects of rotation on this poleward flow, an onshore flow appears. The onshore flow, in turn, induces an E-W pressure gradient which is then balanced by the longshore flow.

The second change appears due to the 45° rotation of the coordinate system. This rotation results in a $\frac{\partial f}{\partial x}$ term which is of the same magnitude and sign as $\frac{\partial f}{\partial y}$. The vorticity equation, in the upper layer, neglecting longshore derivatives in the velocity field, becomes

vy

neglecting longshore derivatives in the velocity field, becomes

$$\frac{\partial}{\partial t}\left(\frac{\partial v_1}{\partial x}\right) + \frac{\partial}{\partial x}\left(u_1\frac{\partial v_1}{\partial x}\right) + f\frac{\partial u_1}{\partial x} + \frac{\partial f}{\partial y}v_1 + \frac{\partial f}{\partial x}u_1 = \frac{\partial}{\partial x}\left(\frac{\tau_{sy} - \tau_{Iy}}{\rho_1 h_1}\right)$$
$$+ A\frac{\partial^3 v_1}{\partial x^3} \tag{23}$$

Upon integration of this equation and the y-momentum equation, and re-calling the fact that the pressure gradient is set equal to zero at the western boundary and that the atmospheric pressure gradient is constant in x, the following relationship is obtained

$$\int_{-L_x}^{x} \beta(v_1 + u_1)dx = g\frac{\partial}{\partial y}(h_1 + h_2 + D)\Big|_x \tag{24}$$

Thus, a N-S pressure gradient is induced by the β effect.

In the downwelling zone, the barotropic Sverdrup balance yields

$$\int_{-L_x}^{x} \beta(v_1 + u_1)dx = g\frac{\partial}{\partial y}(h_1 + h_2 + D)\Big|_x = \frac{\tau_{sy}}{\rho_1(h_1 + h_2)} \tag{25}$$

and in the lower layer the following relationship exists

$$\int_{-L_x}^{x} \beta(v_2 + u_2)dx = g\frac{\partial}{\partial y}(h_1 + h_2 + D)\Big|_x - g'\frac{\partial h_1}{\partial y} \tag{26}$$

Initially, the N-S pressure gradient and atmospheric pressure gradient dominate both layers. Slowly the effects of the wind stress are seen in the upper layer, causing a weakening of the poleward flow and finally an equatorward flow near the coast. Test cases made on the topography of Case III using atmospheric pressure gradient forcing alone and then atmospheric pressure gradient and wind stress forcing, show a more rapid weakening of the flow near the coast in the case with alone and then atmospheric pressure gradient and wind stress forcing, show a more rapid weakening of the flow near the coast in the case with wind stress. Test cases run with a wind stress of 1 dyne/cm^2 and a slightly larger pressure gradient, show a much quicker decrease in the

poleward flow with time resulting from the increase in wind stress. A
test case was also made on topography II with a reverse atmospheric
pressure gradient, showing flows entirely equatorward in both the up-
per and lower layers.

It is of utmost importance to note that when the model was driven
by wind stress only, no poleward flow appeared in either the upper or
lower layer! Thus another type of forcing had to be introduced; the
atmospheric pressure gradient.

b. *Upper Layer Flow*

Study of the upper layer zonal flow reveals quantitative similar-
ities in all three cases. It should be noted here that the solutions
at the northern and southern boundaries in all of the subsequent fig-
ures shown in this paper, have been excluded. The region of particular
interest to this study lies, at most, 100 km to the north and south of
15°S. As previously mentioned in the discussion of bottom topography,
the model has been designed in such a way that the northern and south-
ern most 50 km of the basin are of an artificial nature. Therefore,
the solutions in this region which may contain some effects due to the
model rotation, are, by design, not of importance to this study. Thus
the subsequent figures will range from y = -100 km to y = 100 km only.
The E-W extent of the basin used in the figures will be 100 km from the
coast. This region includes the entire E-W sloping topography and area
of interest to the upwelling system. To avoid confusion, the terms E-W
and zonal refer to the E-W direction in the sense of the model's coor-
dinate system or the onshore-offshore direction. The terms N-S and
and zonal refer to the E-W direction in the sense of the model's coor-
dinate system or the onshore-offshore direction. The terms N-S and
meridional refer to the N-S direction respective to the model or a
longshore direction.

Flows in all three cases are offshore, increasing in magnitude outward into the basin. The major deviation in the zonal flow is seen in Case III, Fig. 8a, over the seamount. North of the seamount axis, the offshore flow increases. Directly over the center of the seamount (x = 15 km, y = -40 km), a stronger offshore flow is seen. These flows may be viewed as compensating for the lower layer zonal patterns in terms of mass continuity. The effects of the seamount topography are seen out into the basin at least 50 km. Peffley and O'Brien (1976) concluded that the longshore dependence of u_1 is mainly dominated by coastline variations. Aside from that due to the seamount, little if any longshore variation is seen in u_1 since the coastline is straight.

Upper layer zonal velocity, as predicted by Ekman dynamics

$$u_1 = \frac{\tau_{sy}}{h_1 f} \approx -.027 \text{ m s}^{-1}$$

seems to be in good agreement with model values. Data taken during JOINT II from buoys at PS and PSS, show an average u value of $-.028$ ms^{-1} at 4 and 12 km offshore and 20 m depth (Halpern - personal communication). The model values also seem to be in close agreement with actual data.

The N-S flow in the upper layer shows similar patterns for all three cases. Initially, all flows are poleward, increasing in magnitude away from the coast. In both topography cases, flows are slightly larger. Topographic features have only a small effect on the upper layer longshore flow. As mentioned in Peffley and O'Brien (1976), the close similarity in the N-S velocity fields between a flat bottom and

close similarity in the N-S velocity fields between a flat bottom and topography case is not due to a lack of effect by the topography, rather a balance between a weaker E-W baroclinic pressure gradient and

Fig. 8a. The zonal component, u_1, of the upper layer velocity for Case III in cm s^{-1}. This figure represents the flow after 5 days of integration. The following convention will be used in this and subsequent figures; dashed lines represent negative contours, solid lines represent positive contours.
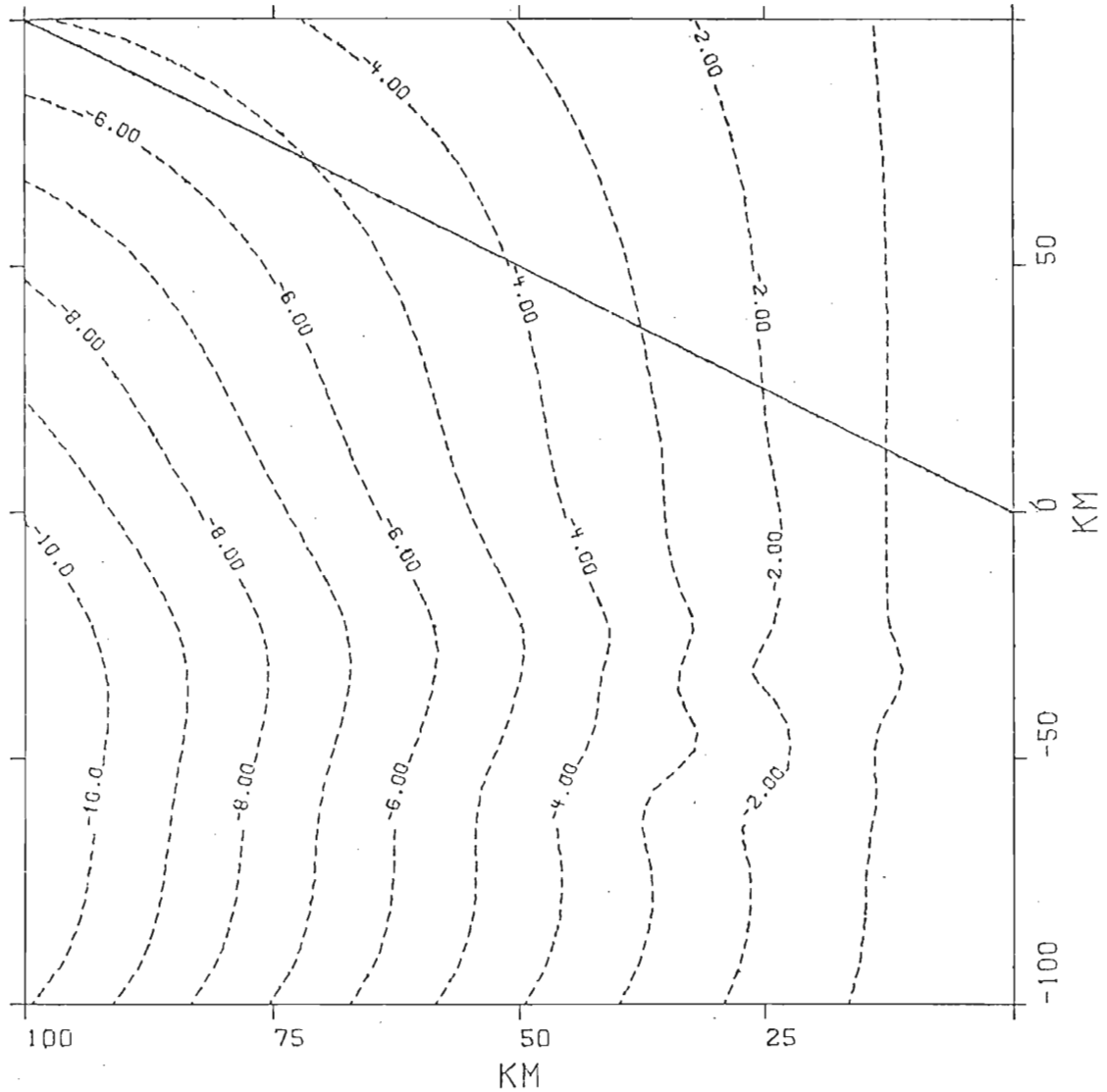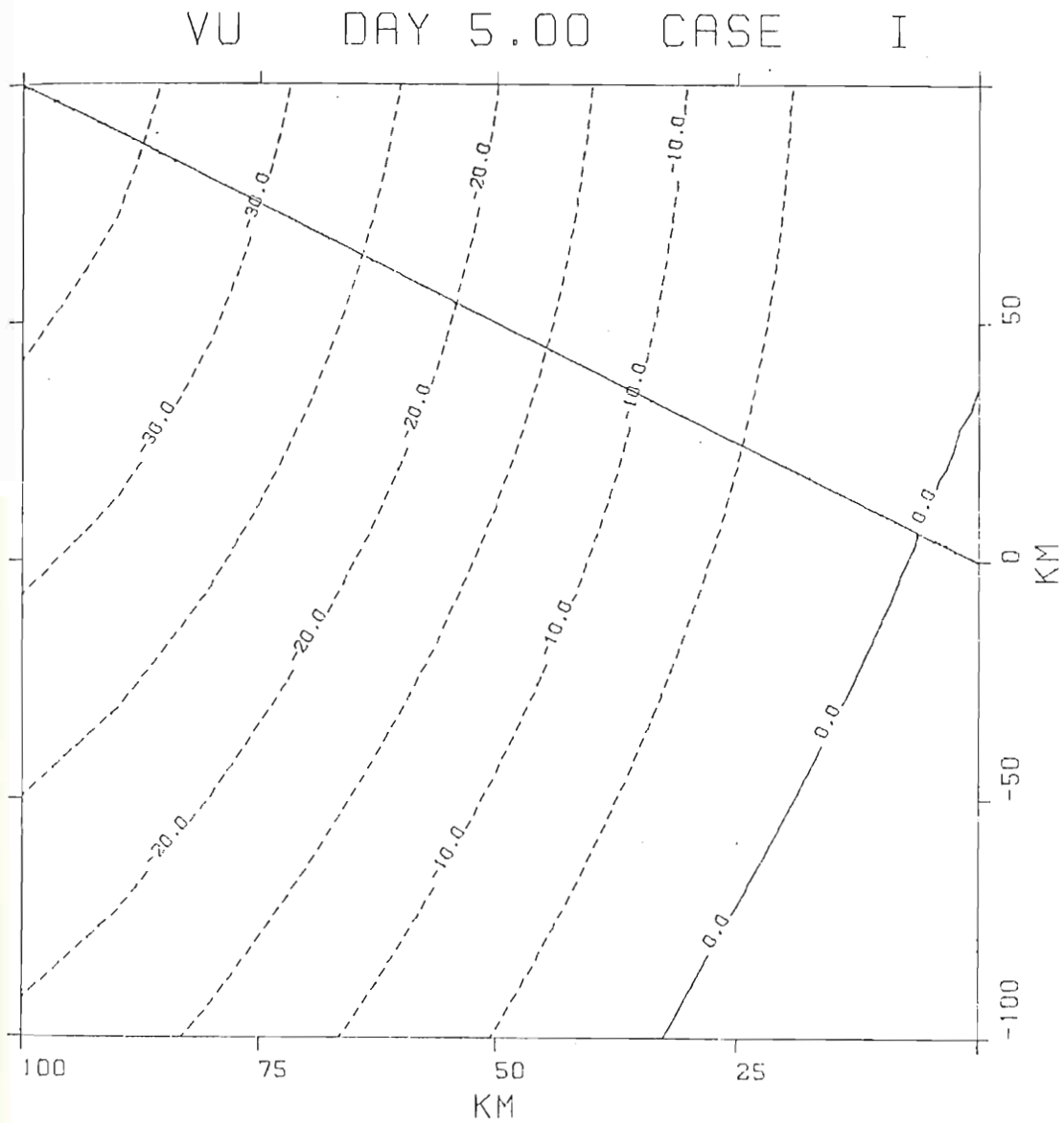
Fig. 8b. The meridional component, v_1, of the upper layer velocity for Case III in cm s^{-1}. This figure represents the flow after 5 days of integration.

stronger barotropic mode in the topography case. The intensity of the
poleward flow, in all three cases, is decreasing with time as the ef-
fects of the wind stress are more strongly felt. At day 5, Fig. 8b, a
small equatorward flow appears at the coast, in all cases, though only
Case I is shown here.

It is also of interest to note that the results observed from two
test cases made using the topography of Case III. One case was forced
only with wind stress, the other with just atmospheric pressure gradi-
ent forcing. The wind stress only case exhibits a totally offshore
flow while the second case showed a weak onshore flow confined to the
coast. The upper layer zonal flows in Case III show the effects of
wind stress dominating in the upper layer. The N-S flows in the wind
stress case show equatorward flows that are far weaker than the pole-
ward flows seen in the atmospheric pressure gradient case. Thus the
N-S flows in Case III are predominantly poleward. These same patterns
appear in Case I and II.

c. *Lower Layer Flow*

The lower layer zonal flow shows important differences among the
three cases. Figs. 9a, b, c represent the lower layer zonal flow at
day 5 for all three cases. In the flat bottom case, the flow is off-
shore with an extremely weak onshore flow near the coast. The flow ex-
hibits a uniform pattern in the N-S direction. As expected, due to the
thickness of the lower layer, the vertically integrated flow is visibly
weaker than in the upper layer.

Case II also shows a weaker offshore flow in the western portion
weaker than in the upper layer.

Case II also shows a weaker offshore flow in the western portion
of the basin than in the upper layer. The most noticeable difference
between this case and the flat bottom case is a distinctive onshore

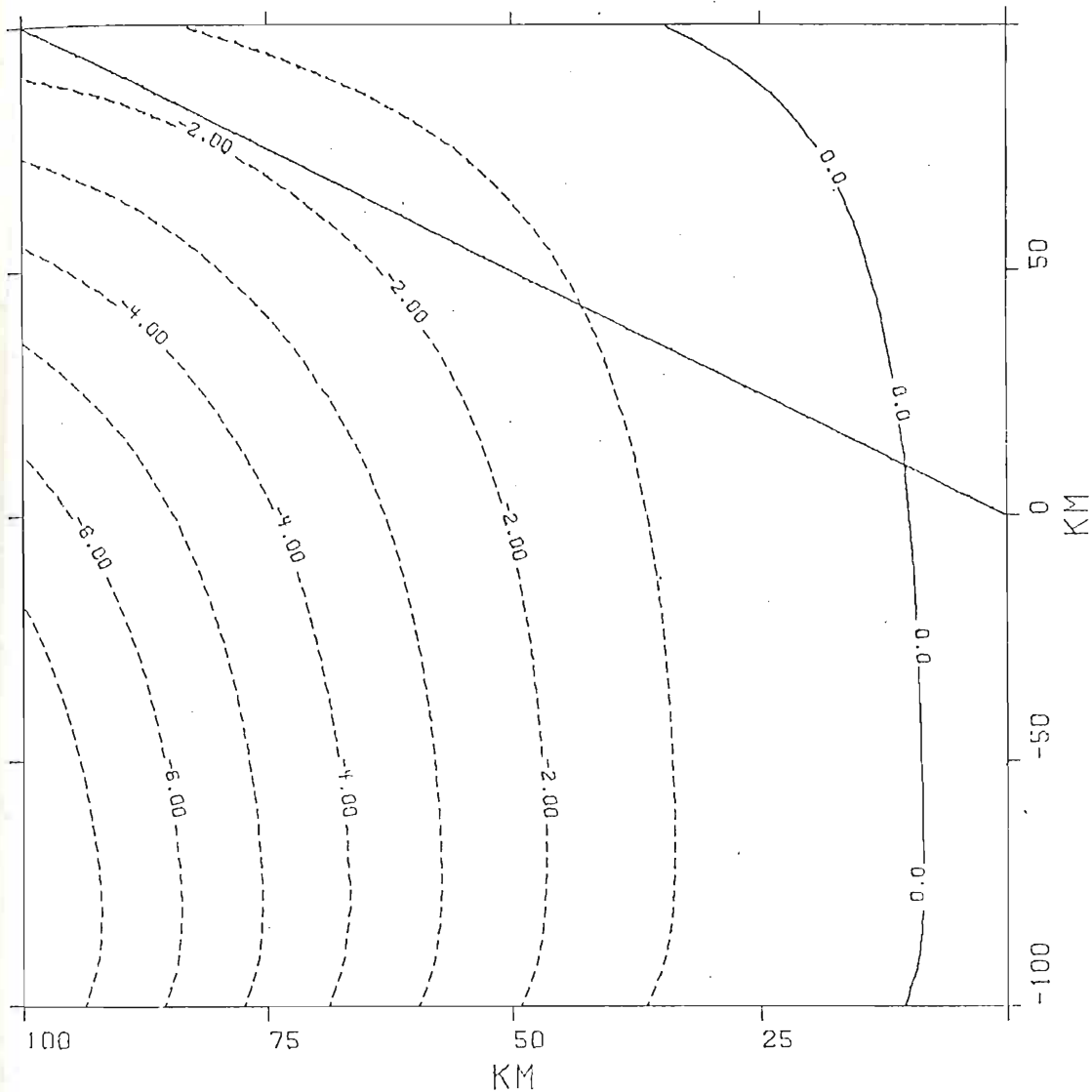Fig. 9a. Zonal velocity, u_2, for Case I. Values are in cm s^{-1} and represent the 5th day of integration.

UL   DAY 5.00   CASE   II
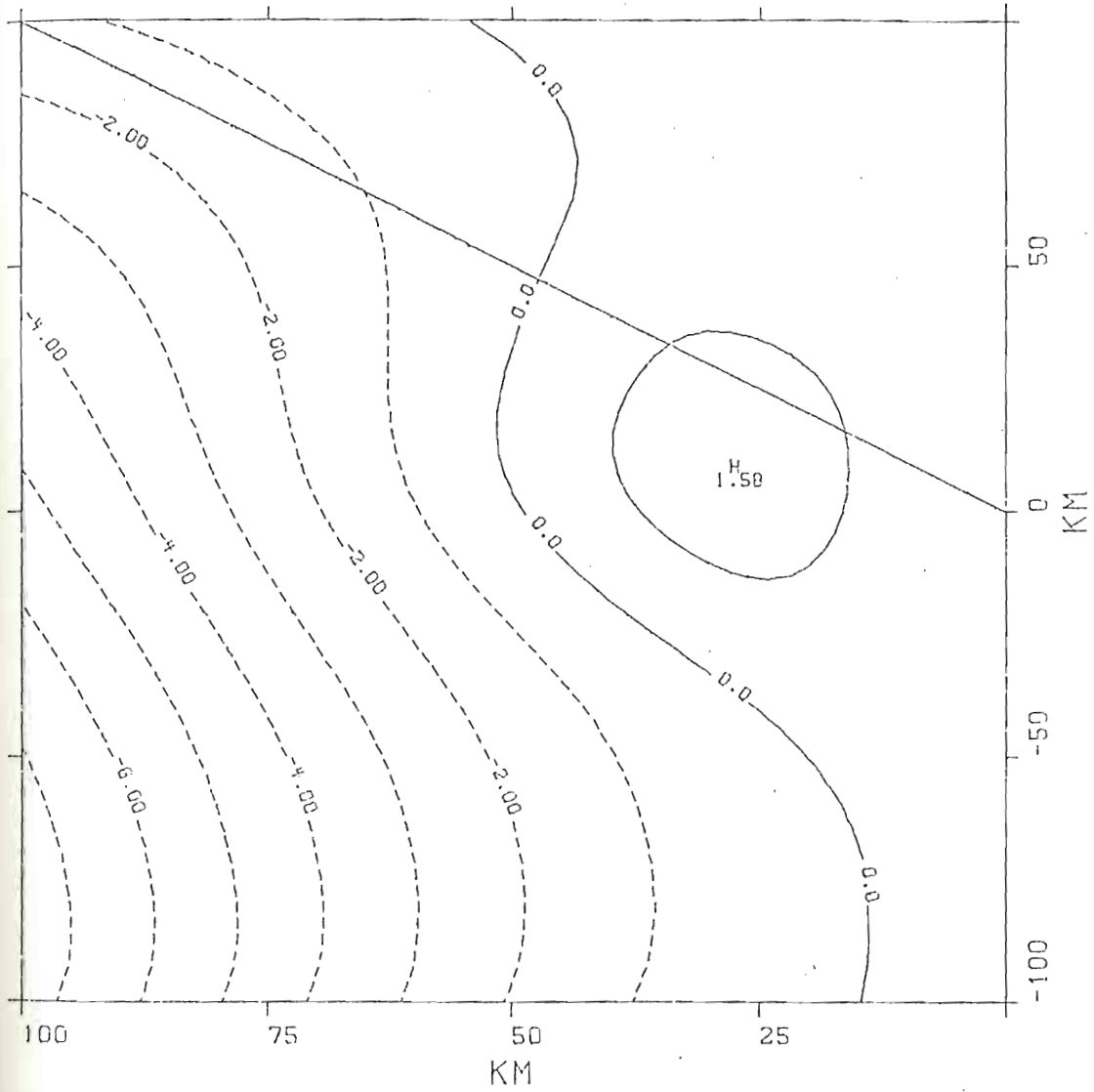

Fig 9b. Zonal velocity, u_2, for Case II. Values are in cm s^{-1} and represent the 5th day of integration.
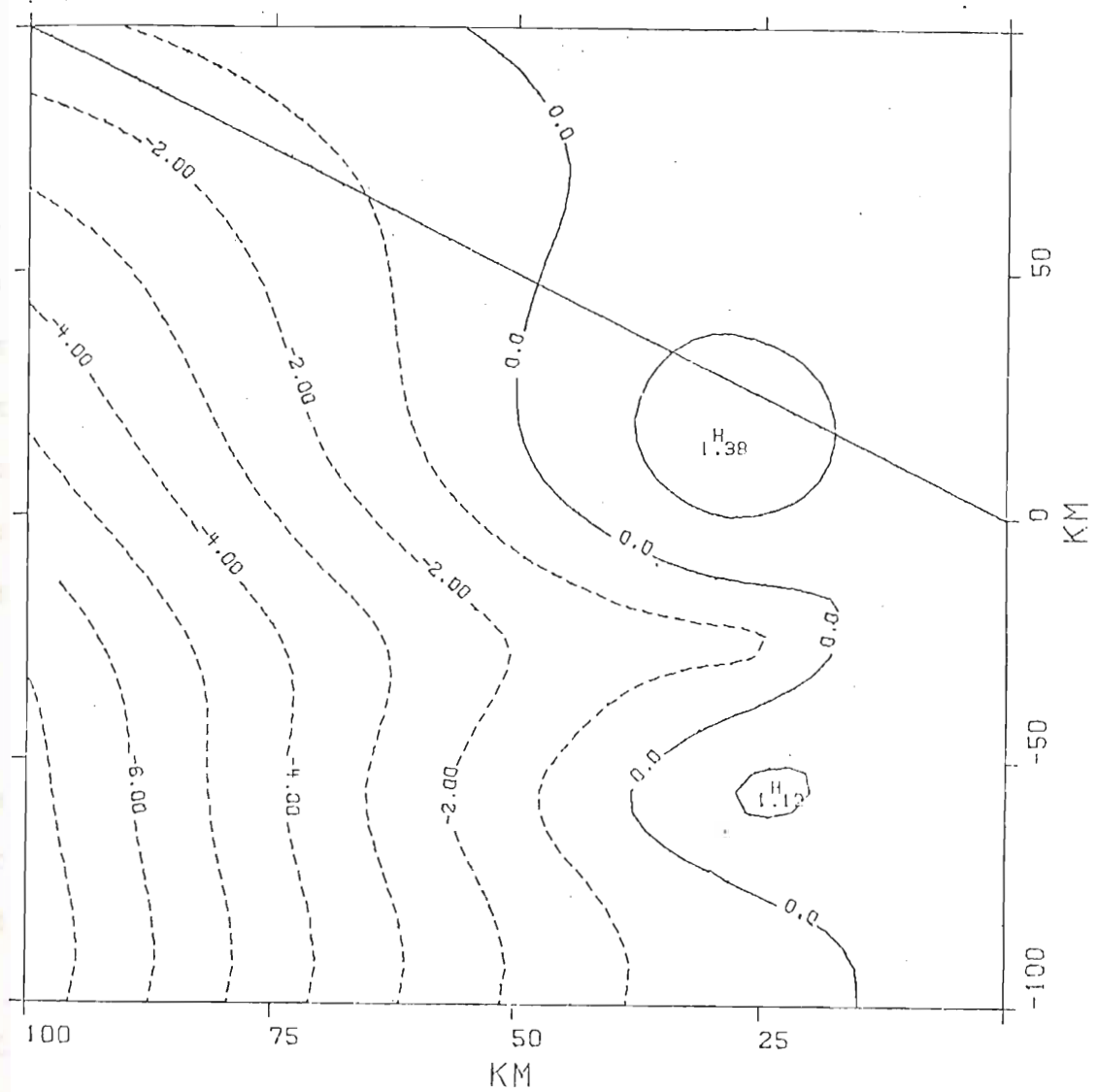
UL. DAY 5.00 CASE III

Fig. 9c. Zonal velocity, u_2, for Case III. Values are in cm s^{-1} and represent the 5th day of integration.

flow near the coast. Fig. 9b clearly shows that topography effects the longshore variations in u_2. The difference between these zonal flows may be explained in terms of mass continuity and a rising topography. Considering the y-momentum equation, Eq. (22b)

$$\frac{\partial v_2}{\partial t} + f\, u_2 = -\frac{1}{\rho^2}\frac{\partial P_a}{\partial y} - g\frac{\partial}{\partial y}(h_1 + h_2 + D) + g'\frac{\partial h_1}{\partial y} - \frac{\tau_{By}}{\rho_2 h_2}$$

and the kinematic boundary condition, $u_2 = 0$ at the coast, it becomes clear that $\frac{\partial v_2}{\partial t} > 0$ for the flat bottom case. This change appears in the model results where the meridional flows become less poleward in time. In the E-W sloping topography case, the interior transport and offshore transport over the shelf are approximately equal. Thus the onshore flow in the lower layer is required to become supergeostrophic by mass continuity forcing $\frac{\partial v_2}{\partial t} > 0$. However, since $f < 0$,

$$\left|\frac{\partial v_2}{\partial t}\right|_{\text{flat bottom}} < \left|\frac{\partial v_2}{\partial t}\right|_{\text{topography}}$$

and therefore, v_2 increases more quickly with time in the topography case until a frictional balance is achieved. Again, the model shows the poleward flow to decrease with time in this case.

The zonal flow in Case III reveals features similar to those in Case II. Again there is a weaker offshore flow to the west than in the upper layer and an onshore flow near the coast. Here however, two maximums of onshore flow appear; one in the same location as the maximum of Case II, and one further south, with a small region of offshore flow between them. These patterns, caused by topographic variations, may still be seen beyond the E-W extent of the topography.

between them. These patterns, caused by topographic variations, may still be seen beyond the E-W extent of the topography.

Before explaining the basic dynamics behind such a pattern of
zonal flow, it will be useful to observe the meridional flow fields for
the three cases. Figs. 10a, b, c show the flows to be poleward in all
three cases. This poleward flow has been documented and discussed by
Smith (1978b), and Brink, et al., (1978). It is also true that the
poleward flow in the lower layer in all three cases is larger than in
the upper layer. Thus the upper layer feels the effects of the wind
stress far greater than the lower layer, as expected. In the northern
portion of the basin, the N-S flows in all three cases are quite simi-
lar with a slightly more poleward tendency in the topography cases.
However, the meridional flows in Cases II and III, deviate from that of
Case I in the region of change in the N-S slope of the topography. Case
II exhibits larger poleward flow in this region and south of this re-
gion than in Case I. A comparison of Case III to Case I shows an in-
crease, a decrease and then another increase in poleward flow when
looking from the northern to the southern portion of the basin. Again,
it is apparent that these flows are topographically induced.

The explanation for these topographically induced variations in
both the zonal and meridional flow fields are based on conservation of
potential vorticity and conservation of mass transport over the sea-
mount. The region of large isobathic gradients in Case II is a region
of maximum onshore flow and decreasing poleward flow. These are the
expected characteristics of flow following the isobaths and conserving
potential vorticity. Case III shows similar flow patterns in the hy-
perbolic tangent region.

potential vorticity. Case III shows similar flow patterns in the hy-
perbolic tangent region.

Two explanations may be given for the alongshore variations in
both zonal and meridional flow near the seamount. In this region as

Fig. 10a. Meridional velocity, v_2, in cm s^{-1} for Case I.
These solutions are representative of 5 days of integration.

VL   DAY 5.00   CASE   II

Fig. 10b.   Meridional velocity, v_2, in cm s^{-1} for Case II. These solutions are representative of 5 days of integration.

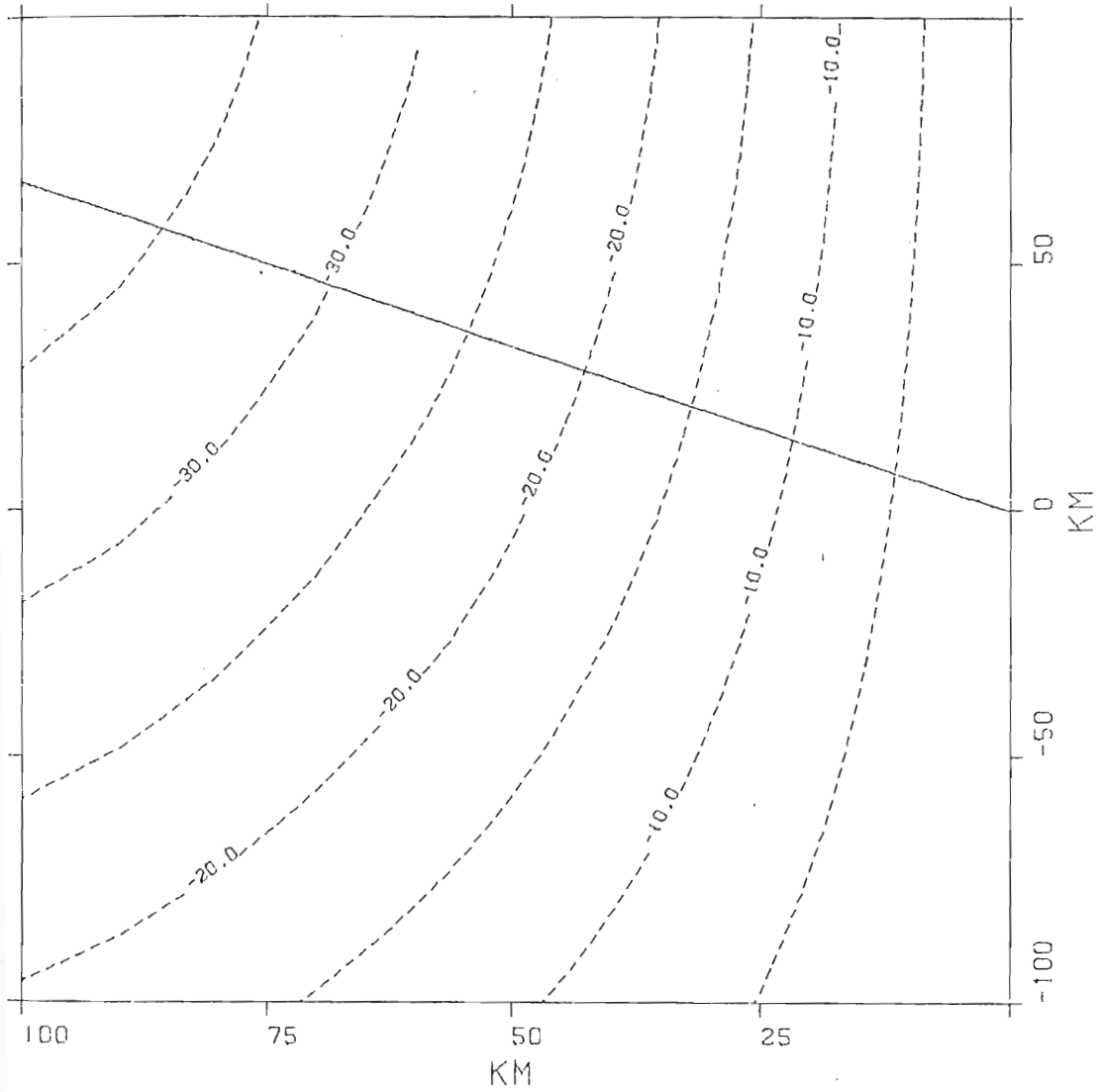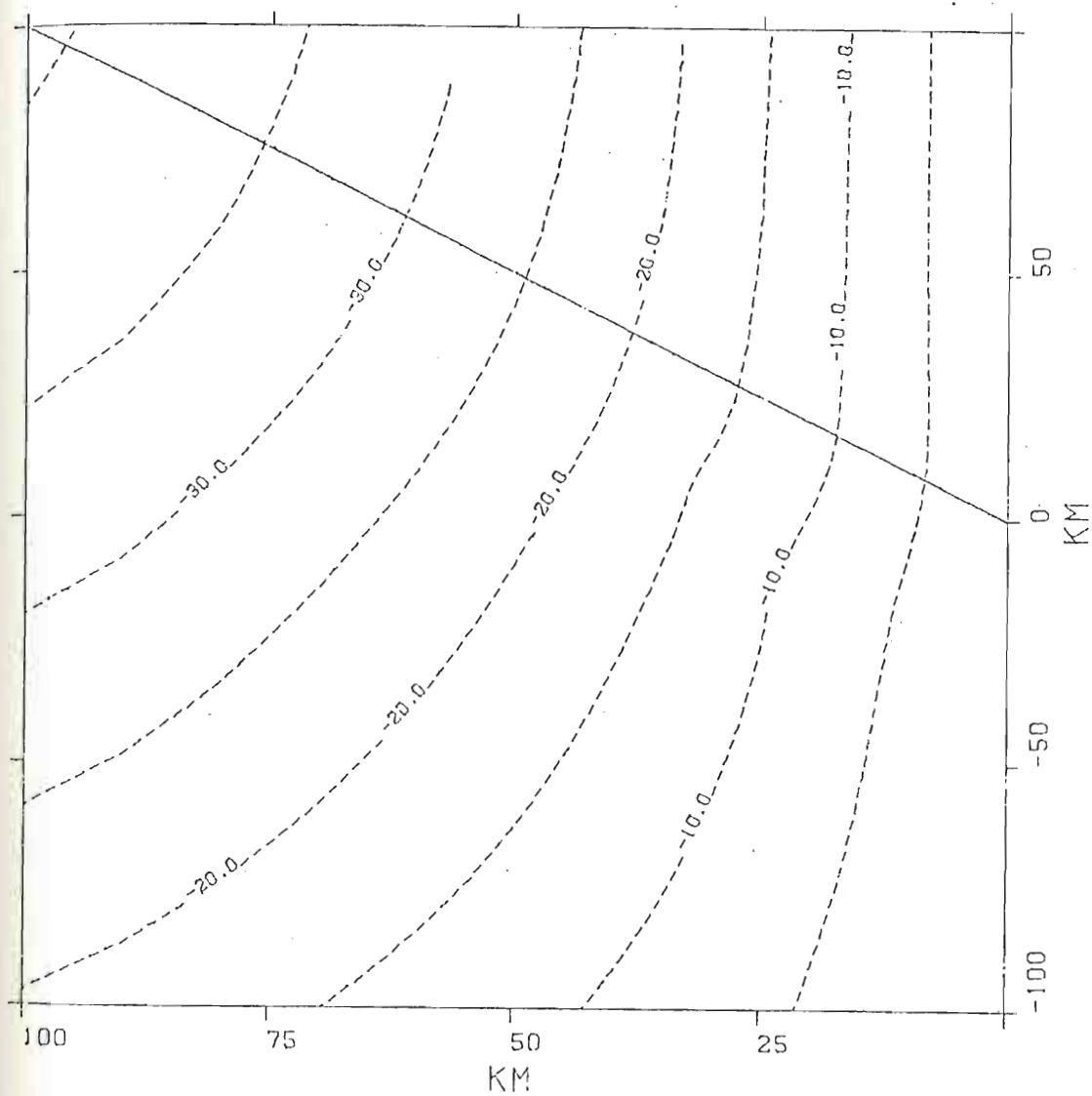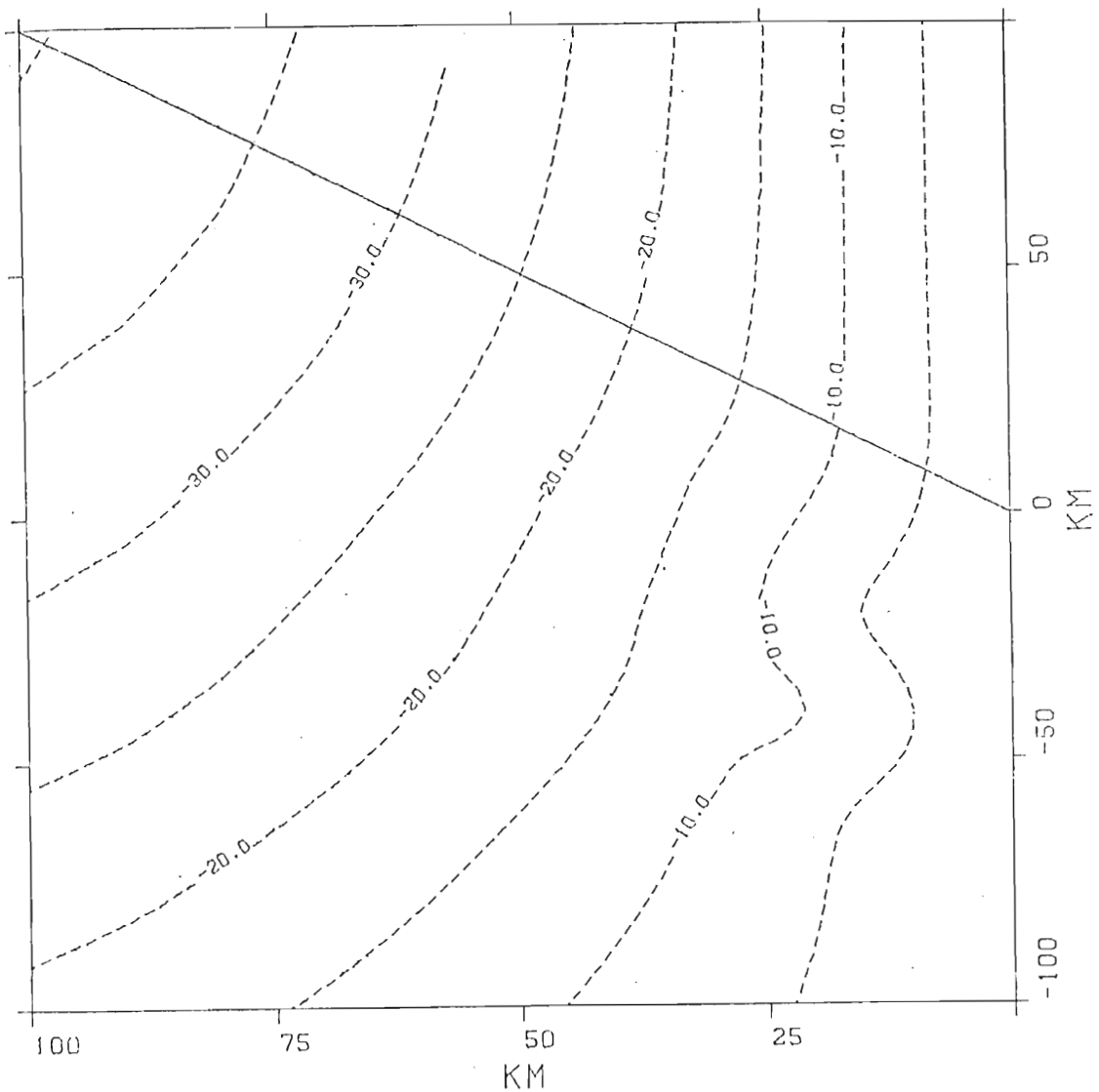Fig. 10c. Meridional velocity, v_2, in cm s^{-1} for Case III.
These solutions are representative of 5 days of integration.

well as the hyperbolic tangent region, flow follows the isobaths. In the northern half of the seamount, where isobaths turn toward the interior of the basin, flow decreases in the onshore direction and increases in the poleward direction. When the isobaths turn toward the coast on the southern half of the seamount, flow increases in the onshore direction and decreases in the poleward direction. These large alongshore variations may also be explained as due to a conservation of mass transport. North of the seamount, the lower layer depth, h_2, increases. Flow in this region slows down, becoming smaller in magnitude in both onshore and poleward flow. Rising over the seamount, where lower layer depth, h_2, decreases, the flows increase in magnitude in both the onshore and poleward directions. When the layer thickens south of the seamount, flows decrease once again.

One final general feature of the zonal flow is apparent in all three cases; the E-W extent of the onshore flow is larger in the northern portion of the basin than the southern portion of the basin. This characteristic may be explained simply as due to the effects of geostrophy on the lower layer zonal flow. As stated in the discussion of the dynamics on a β plane, u_2 is in geostrophic balance. Thus u_2 varies inversely with f and would be expected to increase when approaching the equator.

d. *Upwelling*

It is of utmost importance to this study to note the differences in amounts of upwelling due to the different topographic features. Figs. 11a and 11b, show the upwelling patterns for Cases I and II. The in amounts of upwelling due to the different topographic features. Figs. 11a and 11b, show the upwelling patterns for Cases I and II. The amounts of upwelling are also referred to as the pycnocline height
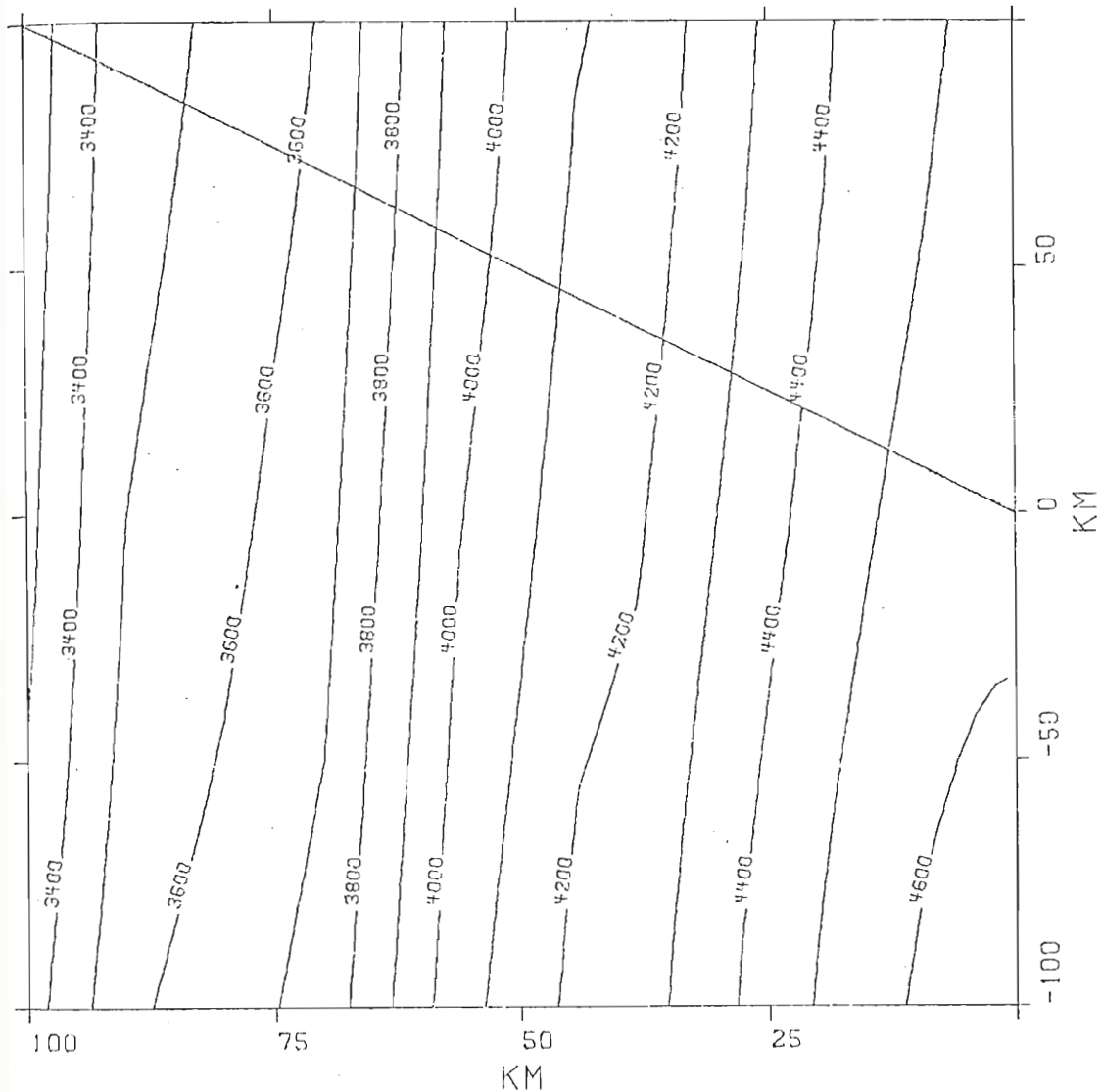
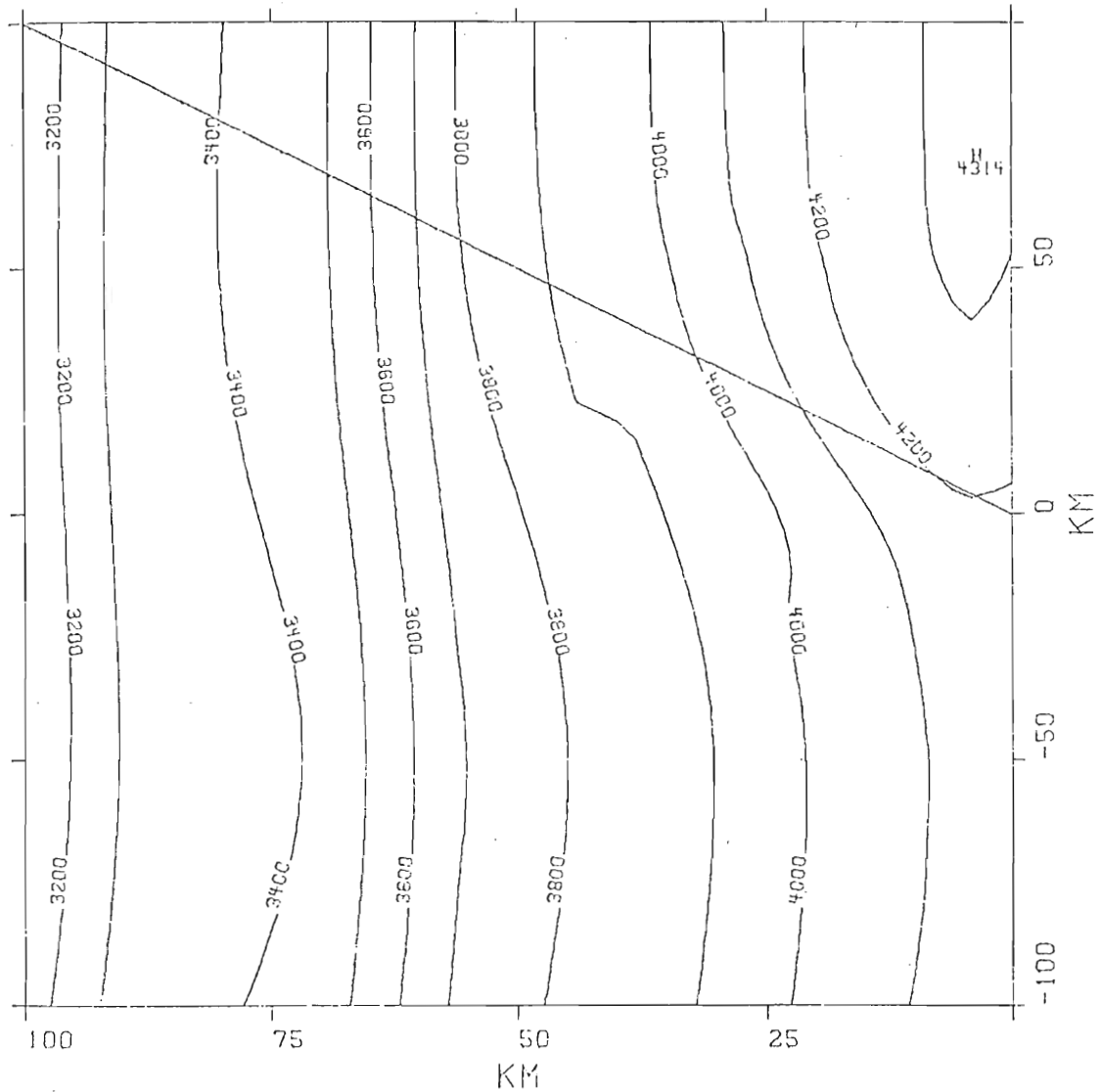Fig. 11a. Contours of the pycnocline height anomaly at day 5 for Case I. Contour values are in cm.

Fig. 11b. Contours of the pycnocline height anomaly at day 5 for Case II. Contour values are in cm.

anomaly, which describes the displacement of the layer interface from its initial position.

The flat bottom case shows a simple upwelling pattern with increasing amounts of upwelling close to shore. By day 5, an average of 45 m of upwelling is seen at 25 km with a maximum of 46 m closer to the coast. Longshore upwelling is rather uniform in appearance.

Case II does not reveal a uniform longshore pattern. Instead, a maximum now appears at y = 50 km, over the broad shelf region of the topography. This characteristic is apparent across the basin where amounts of upwelling are larger in the north than the south. Recall that in the region of broad shelf the zonal flow was onshore and poleward flow larger than in the south. Thus the tendency observed in Peffley and O'Brien (1976), for regions of larger poleward flow to also be regions of larger upwelling and an increased baroclinic mode, is also observed in this model. The amount of upwelling increases rapidly near the 15° south line and an x value of 25-15 km. This increase, seen in both Figs. 11b and 13a, is located in the region of maximum onshore and poleward flow. Fig. 12 shows the difference in the amounts of upwelling between Case I and II. The topography case exhibits weaker upwelling near the coast, due to upwelling induced further out into the basin by the E-W sloping topography. The region of the most drastic change in these upwelling differences appears in the region of largest change in: N-S slope of the topography, the lower layer zonal flow and the lower layer meridional flow, as expected.

Perhaps the figures of most interest are Figs. 13a and 13b. Fig. 13a is the amount of upwelling for day 5 obtained from the model for

Perhaps the figures of most interest are Figs. 13a and 13b. Fig. 13a is the amount of upwelling for day 5 obtained from the model for Case III. Fig. 13b is a representation of mean sea surface tempera-
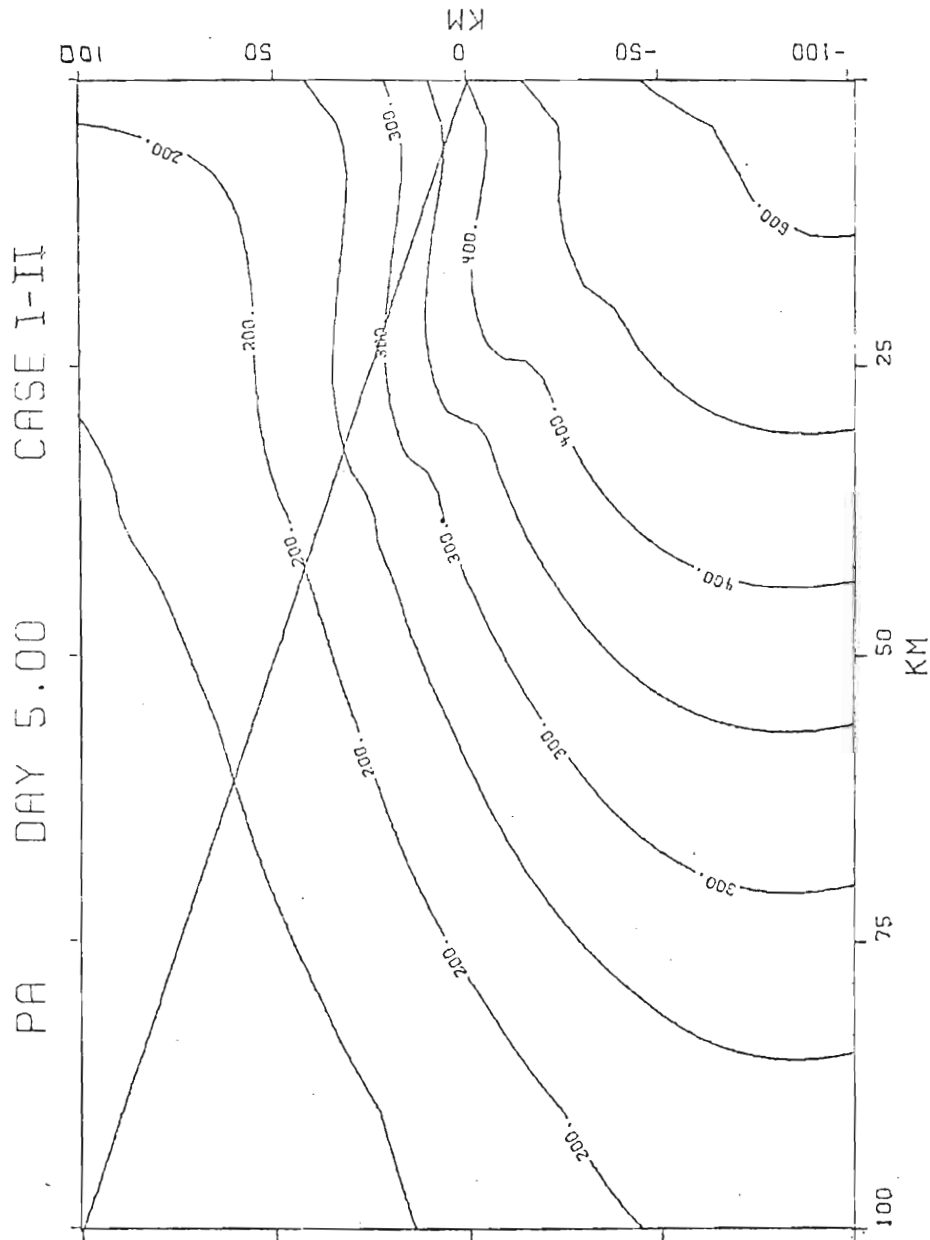
Fig. 12. Contours of the difference in the pycnocline height anomaly for Case I-II. Contour values are in cm.
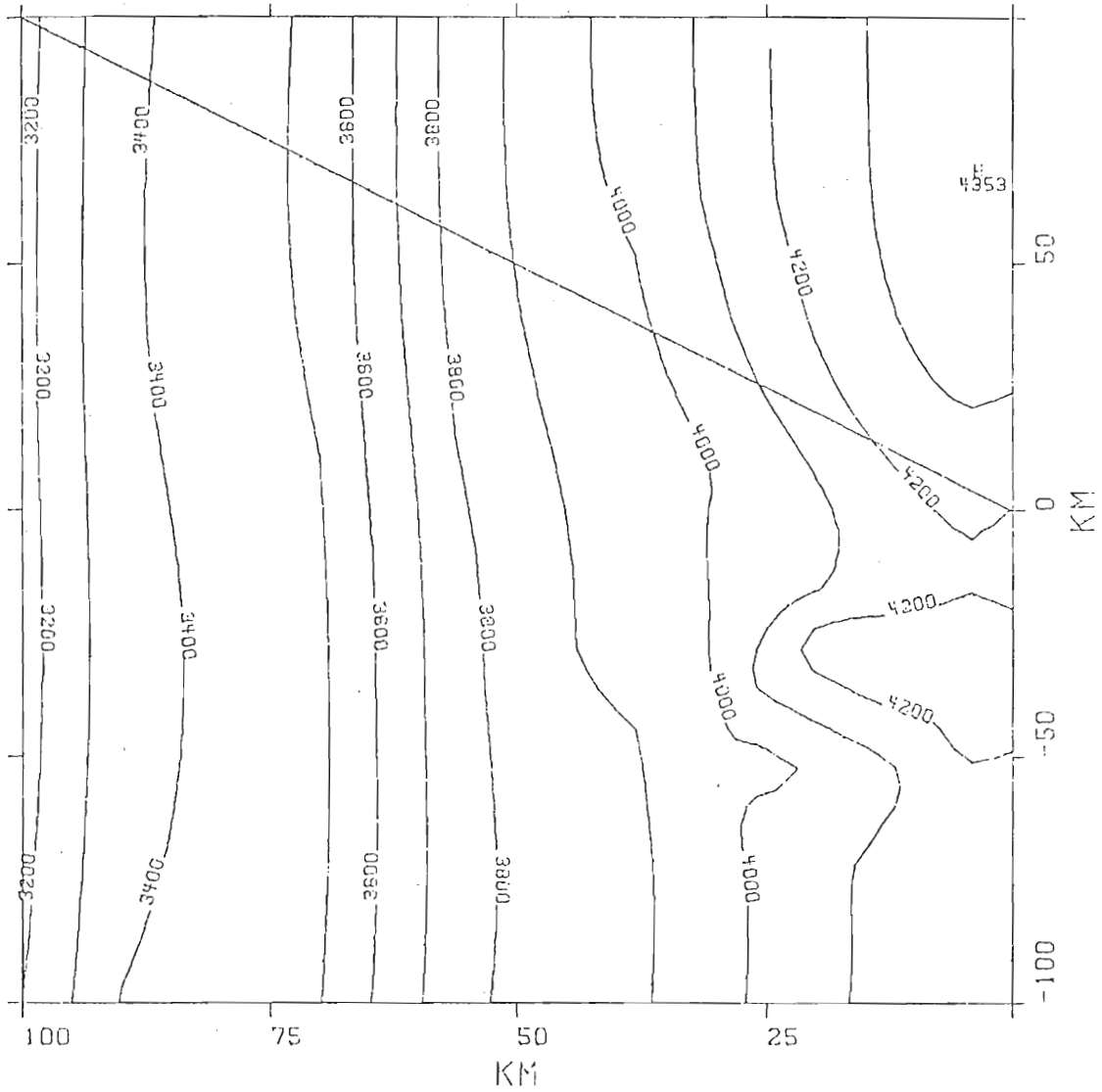
Fig. 13a.   Contours of the pycnocline height anomaly for Case III.   Contours are in cm.
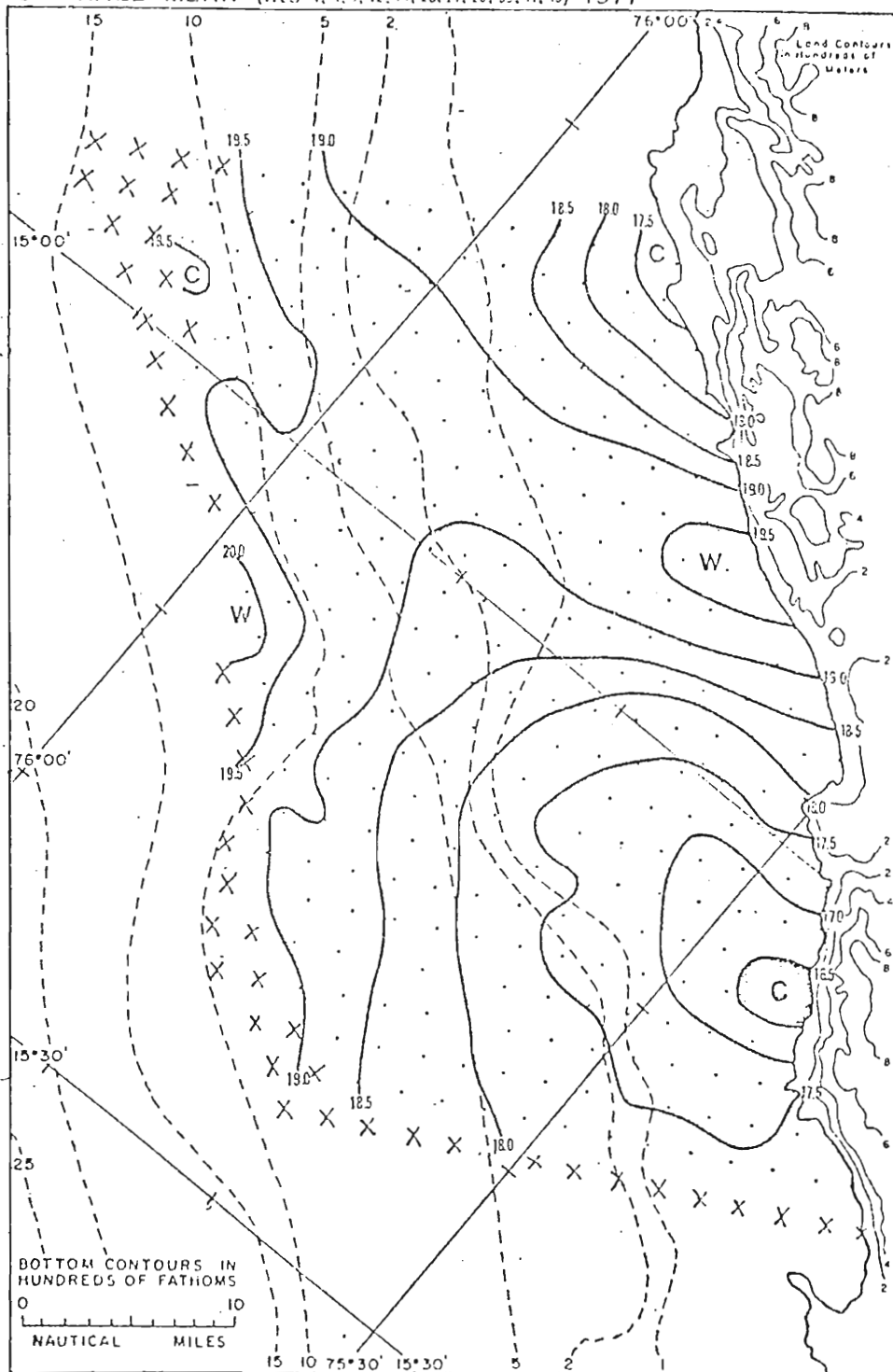
Fig. 13b. Mean sea surface temperatures from JOINT II 1977 data from Stuart and Nanney (1978). Contours are in degrees of centigrade.

tures in the JOINT II region of research from Stuart and Nanney (1978).
Regions of largest upwelling coincide with regions of coldest tempera-
tures while upwelling minima   coincide with warm areas. Case III
shows regions of largest upwelling agree fairly well with the mean map.
The maximum cold temperature lies approximately 35 km north of 15°S,
while the model predicts a maximum at approximately 50 km. The second
maximum lies approximately 13 km south of 15°S while the model predicts
the maximum to be near 30 km south of 15°S. The upwelling minimum also
appears south of the warmest temperatures. The fact that these highs
and lows of upwelling do not exactly coincide is due to the fact that
the topography in Case III, though a close estimate to the actual
topography, is still idealized. Thus, similar but not exact results
are expected.

Fig. 13a exhibits the maximum in the north as expected from the
results of Case II. The new feature is the addition of another maximum
in the region of the seamount and a resulting relative minimum in the
region between the two maxima. The minimum occurs in the region just
below the 15°S line where the flow becomes less poleward. The highest
values occur where the flow becomes more poleward, again resulting in
an increased baroclinic mode. Perhaps a simpler way to view the cause
of these minima and maxima of upwelling is to think of the lower
layer flow coming from the north and being forced to rise over the sea-
mount, thus inducing more upwelling just north of the seamount and less
upwelling south of the seamount.

The difference between the pycnocline height anomaly fields of

The difference between the pycnocline height anomaly fields of
Cases I and III and Cases III and II are shown in Figs. 14a and 14b.
Case III also shows less upwelling near the coast. This again is ex-
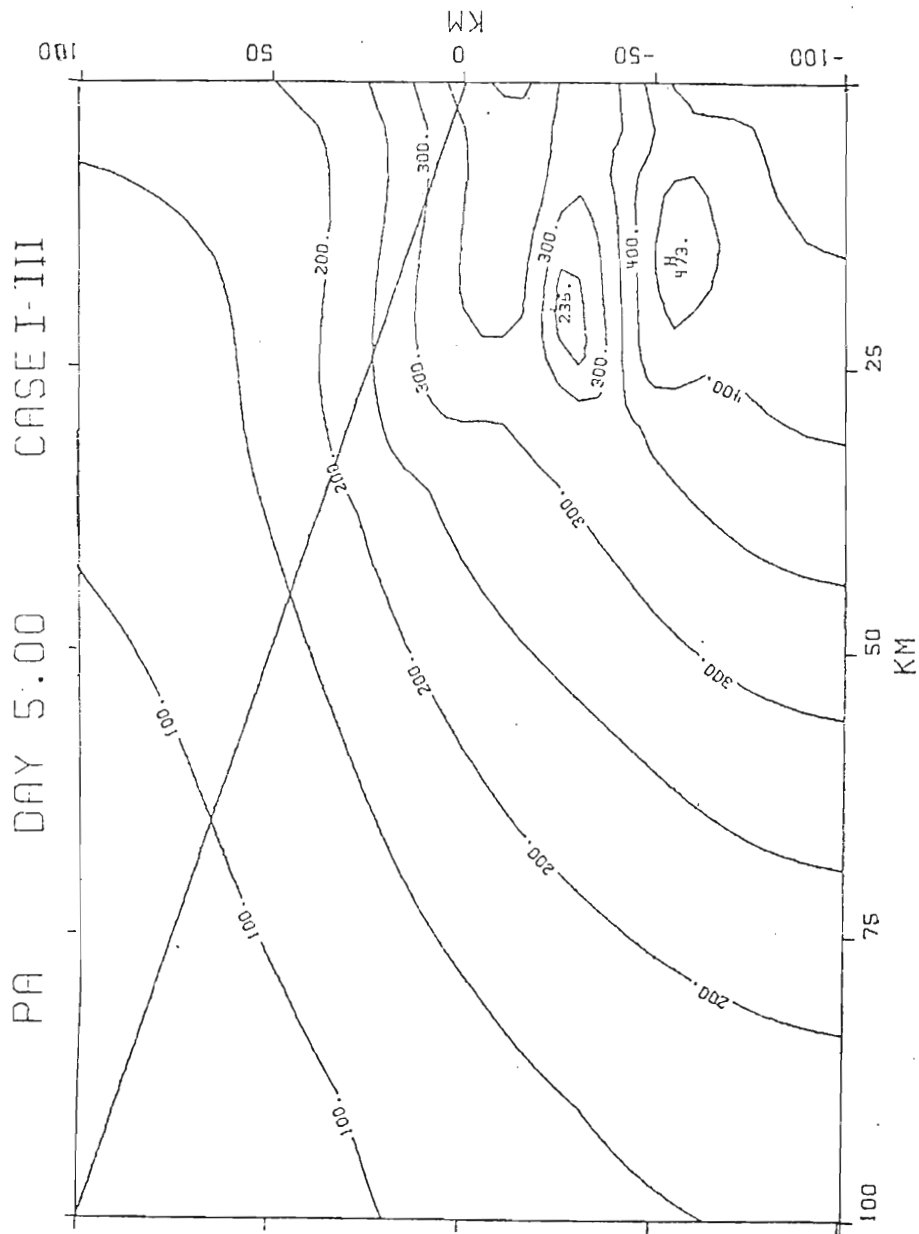
Fig. 14a. Contours of the difference in the pycnocline height anomaly
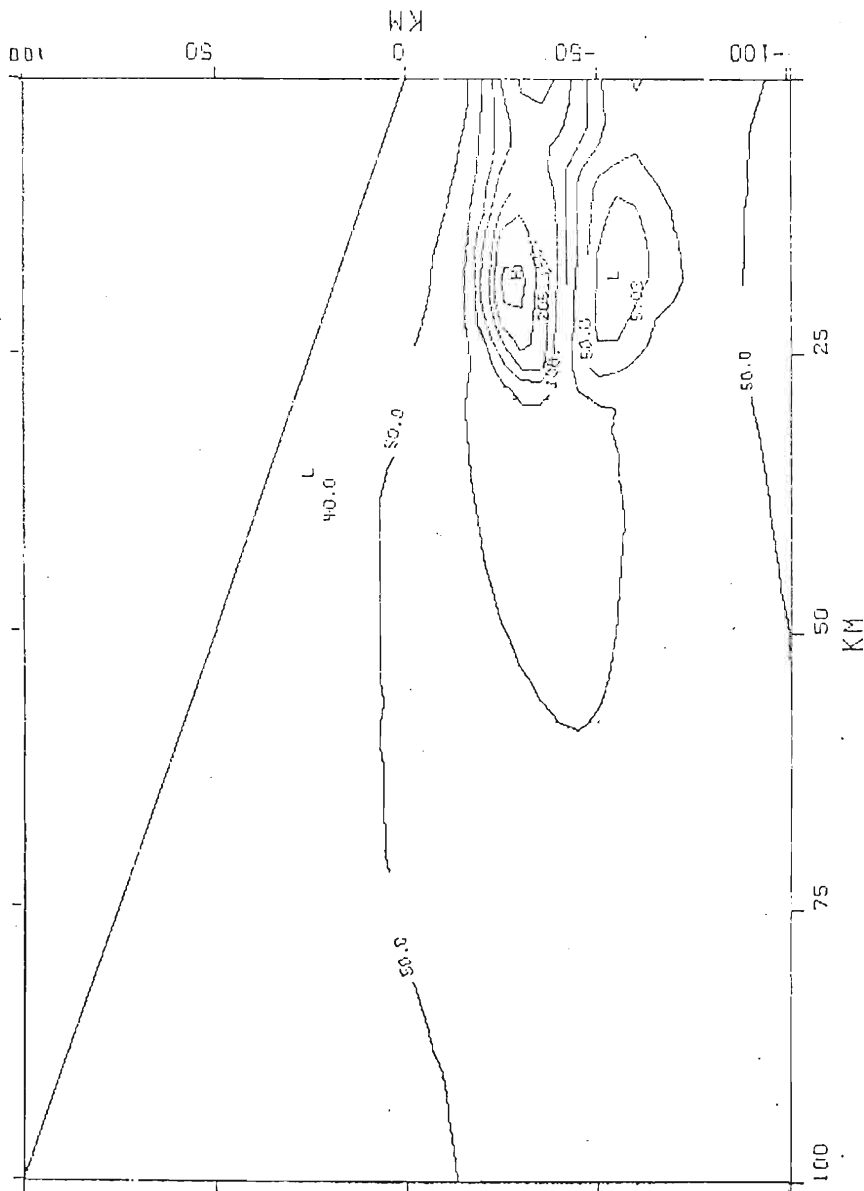for Cases I-III. Contour values are in cm.

Fig. 14b. Contours of the difference in the pycnocline height anomaly for Cases III-II. Contour values are in cm.

pected due to the introduction of a sloping topography. In general, the amounts of upwelling in Case III and Case II differ only in the 50 km nearest the coast with Case III having slightly more upwelling. Both figures reveal that Cases II and III are quite similar in the upper half basin. However, the differences in upwelling due to the introduction of the seamount is obvious in both figures. Thus a mesoscale topographic feature appears responsible for some definite changes in the upwelling pattern.

From the results of Cases II and III, favored areas of upwelling seem to be over the broad shelf and very slightly north of the seamount's center. Upwelling contours appear to parallel the isobaths in most regions. Also the longshore and offshore scales both seem to be based on the scale of the topography. Thus here, as in Peffley and O'Brien (1976), it is the topographic variation that dramatically affects the upwelling pattern.

e. *X-Z Cross Shelf Section*

Cross sectional analyses of the zonal and meridional flows, along the "C" Line (see Fig. 3), for the JOINT II project were done by Van Leer (1979) from cyclosonde data. Figs. 15a and 15b show the meridional field in cross section based on cyclosonde data from Van Leer for May 28 and May 31, 1976. Initially, the flow is all poleward, weak in the upper layer and increasing with depth and weakening over the shelf. As time goes on, the flow becomes less poleward near the coast, until finally, after 5 days, a strong equatorward flow is established in the region nearest the coast while poleward flow is found only furuntil finally, after 5 days, a strong equatorward flow is established in the region nearest the coast while poleward flow is found only further out on the shelf.

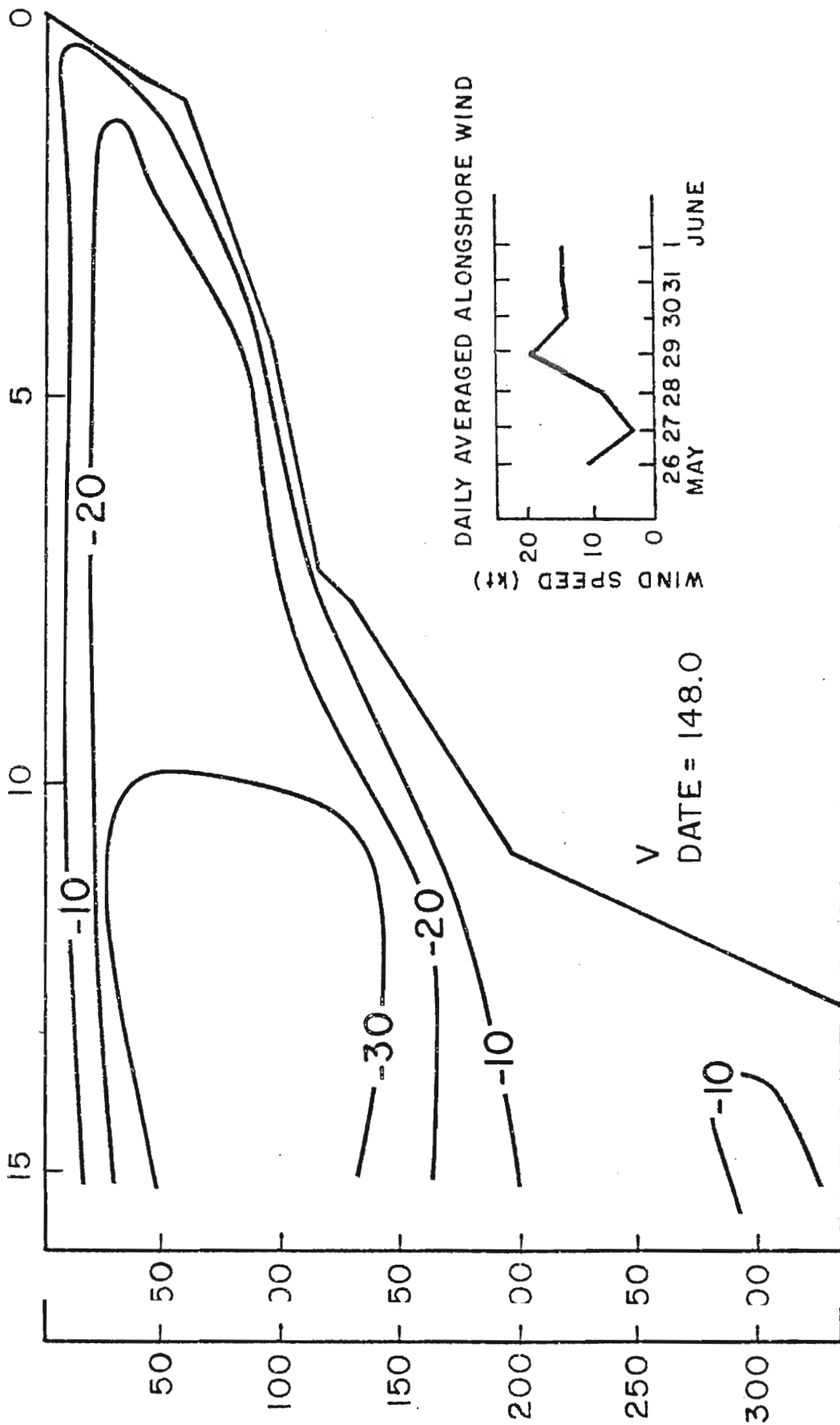Fig. Fig. 15a. Contours of meridional velocity in vertical cross section given in cm s^{-1} as obtained by Van Le Van Leer (1979) from cyclosonde data. This figure represents May 27, 1976.
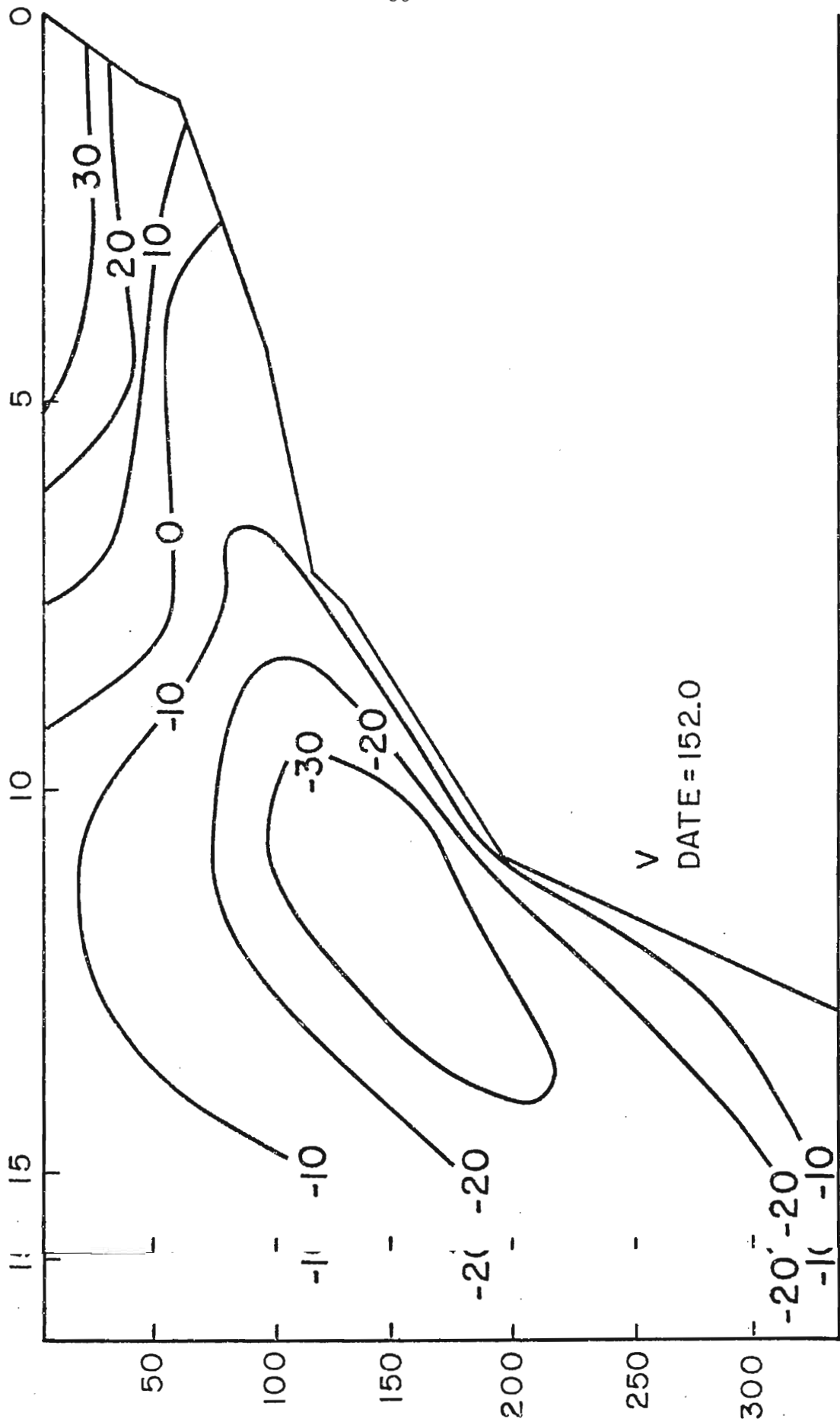
Fig. 15big. 15b. Contours of meridional velocity in vertical cross section in cm s^{-1} as obtained by Van Leer (197er (1979) from cyclosonde data. This figure represents May 31, 1976.

The model shows quite similar results. Fig. 16a depicts a small equatorward flow in the upper layer near the coast with poleward flow below and further out into the basin. The magnitude of the poleward flow decreases rapidly towards the surface. Thus large velocity gradients are created in the upper layer indicative of the dominance of the baroclinic mode. In the lower layer, the flow takes on barotropic features changing little with depth. As time goes on, Fig. 16b, the equatorward flow is seen to strengthen and expand further into the basin. The magnitude of the meridional velocity weakens rapidly close to the shelf due to the boundary conditions. The observed data exhibits this same feature.

There is some discrepancy between the model and real data when considering the magnitudes of the flows. The intensity of the equatorward coastal flow in the model is approximately five times weaker than the observed flow. This could be partly explained by the low value of wind stress chosen for the model. The poleward flow also seems generally a bit weaker, however the magnitudes of the meridional velocity in Fig. 17b may be slightly large as the next day's data show a considerable drop in the magnitude to approximately -10 cm s^{-1}. Thus discrepancies in the magnitudes of the poleward flow may be far smaller than the comparison of Fig. 15b and 16b reveal.

Based on Van Leer's data, a cross section of the zonal component of the velocity for May 27, 1976, is shown in Fig. 17. An offshore flow, which deepens away from the coast, is observed in the upper layer. At approximately 50 m depth, an onshore flow of larger magnitude dominates. This flow is expected to occur due to the effects of rotation on the type of prodominant poleward flow seen in the four previous figures.

Fig. 16a. Contours of meridional velocity in vertical cross section at day 2.5 from model Case III. Vail. Values are in cm s^{-1}.
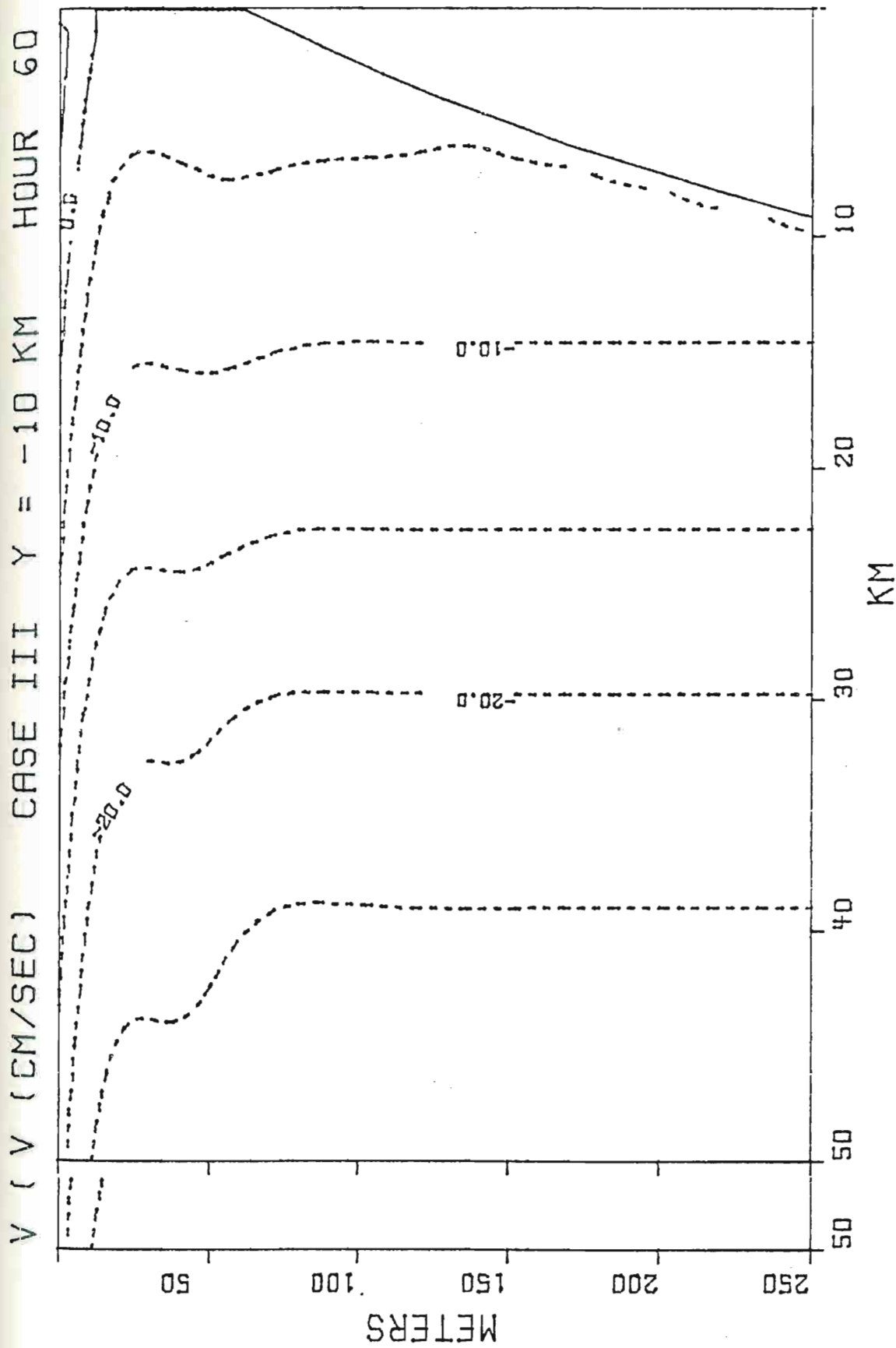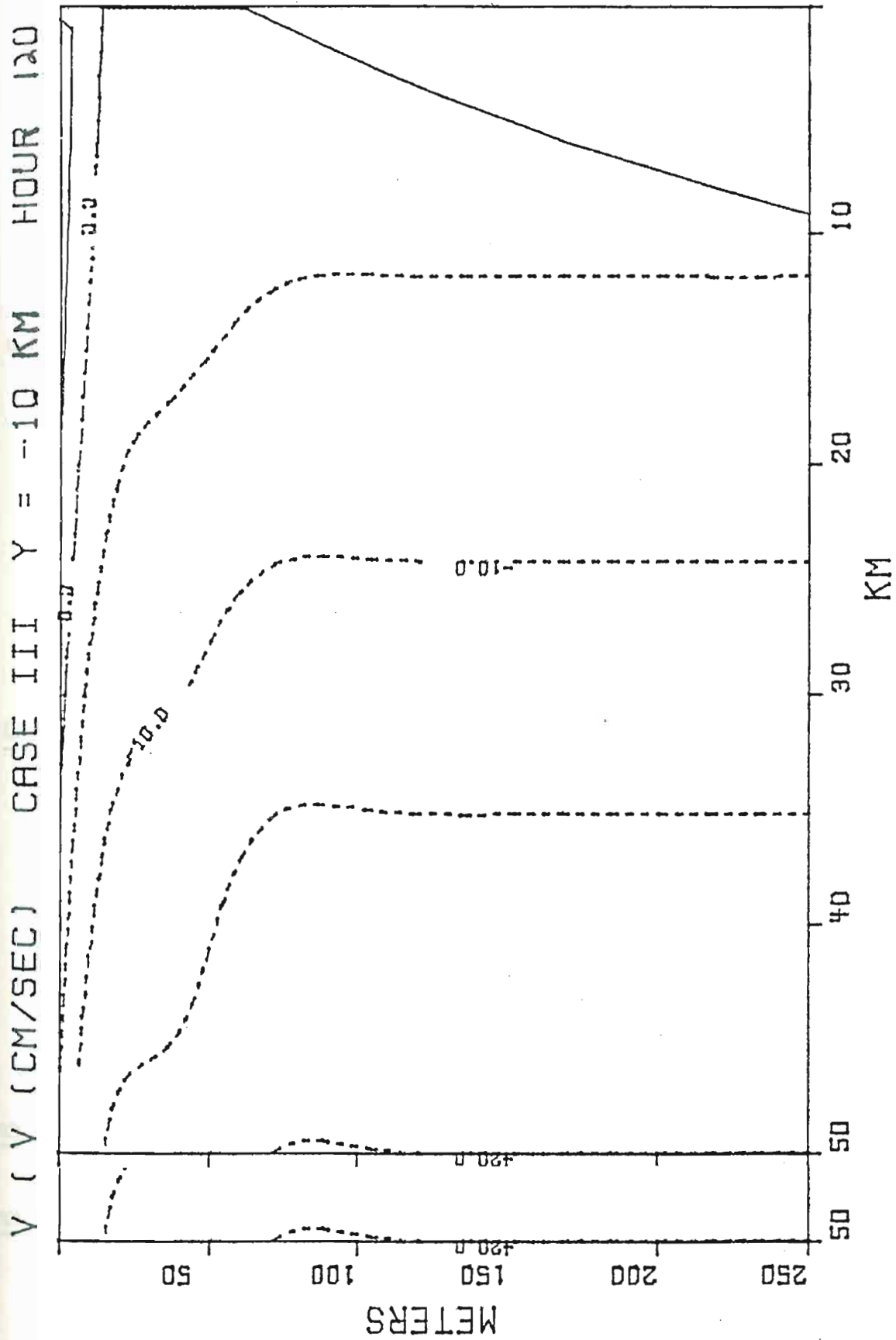
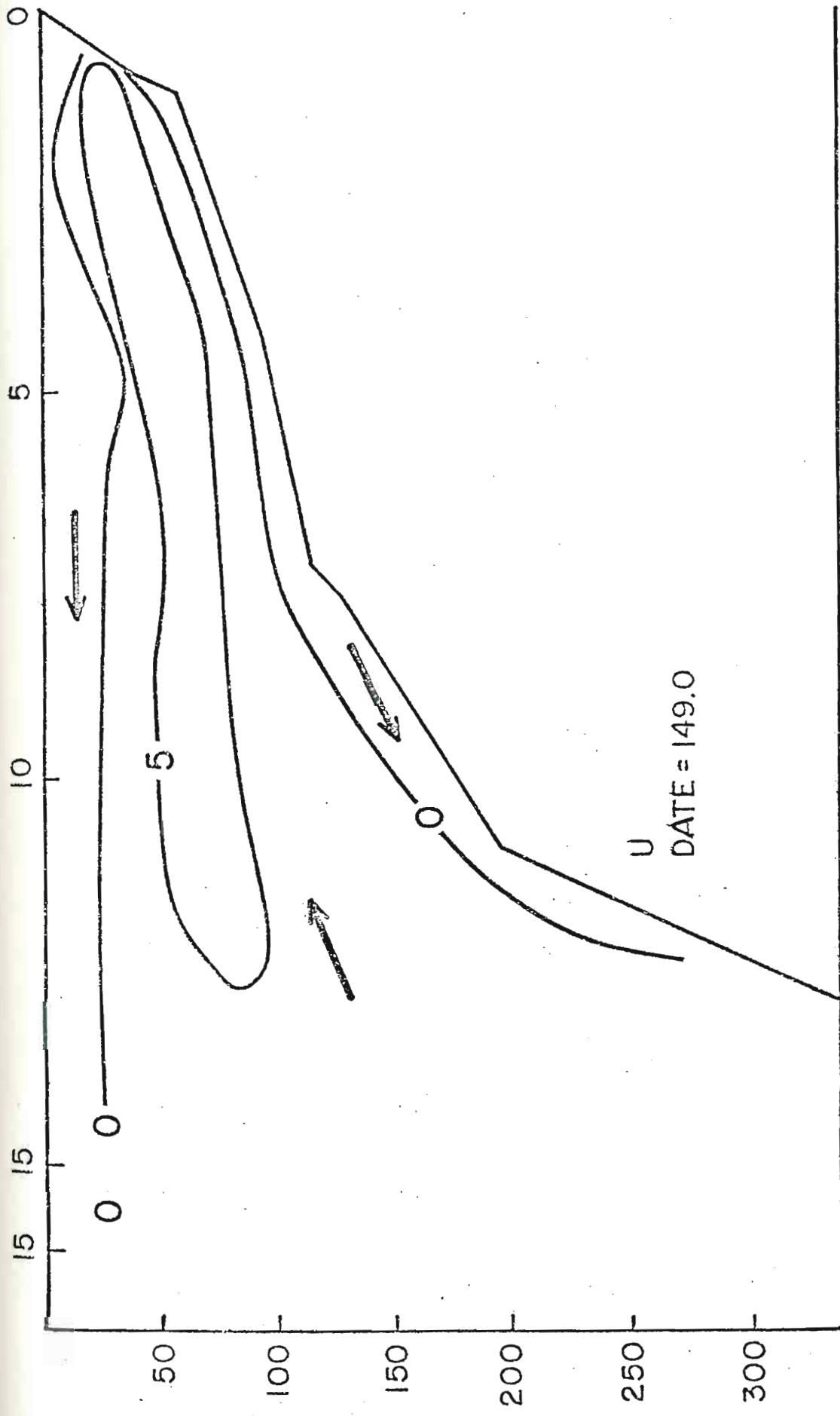Fig. 16b. Contours of meridional velocity in vertical cross section at day 5 from model Case III. Values are in cm s^{-1}.

Fig. 17. Cro7. Cross shelf contours of zonal velocities in cm s⁻¹ obtained from cyclosonde data by Van Leer (1979). 979). This figure represents May 28, 1976.

The onshore flow weakens approaching the shelf, and a weak offshore flow appears in a narrow region over the shelf.

The appearance of this offshore flow near the shelf has also been seen by O'Brien et al.,(1979) in calculations done for an adjusted u field and vertical velocities. Fig. 18 is the calculation of the velocity fields for April 11, 1976, obtained using this adjusted u field. Note an offshore flow near the coast at 4, 12 and 20 km. Also note the thickening of the offshore layer with distance from the coast as observed by Van Leer. At approximately 40 km depth, the flow becomes onshore and remains so until very near the shelf.

The cause of this reversal in flow at the bottom is due to an Ekman boundary layer. In the lower layer, the flow is geostrophically balanced. Close to the bottom, viscous terms become large, reduce the Coriolis effect and cause an offshore veering, or a reversal in the zonal flow. The depth of this layer, from Ekman dynamics and using the value of vertical eddy viscosity chosen in this model, is $\simeq$ 16 m. This is in good agreement with the observed value from Fig. 17 which shows an average depth between 15 and 16 m.

Figs. 19a-d show the zonal velocity field derived from this model using the x-z cross section method of Thompson previously described. In all four locations the upper layer flow is offshore, increasing in its western extent with time. It is also interesting to note that the thickness of the layer increases away from the coast as seen in the actual data. This thickening of the upper layer offshore is due to the effects of the atmospheric pressure gradient. In test cases made using only atmospheric pressure gradient forcing, onshore flow appears near effects of the atmospheric pressure gradient. In test cases made using only atmospheric pressure gradient forcing, onshore flow appears near the coast, decreasing in value to about 25 km into the basin and then

Fig. 18. Vertical cross shelf plot of adjusted u and w
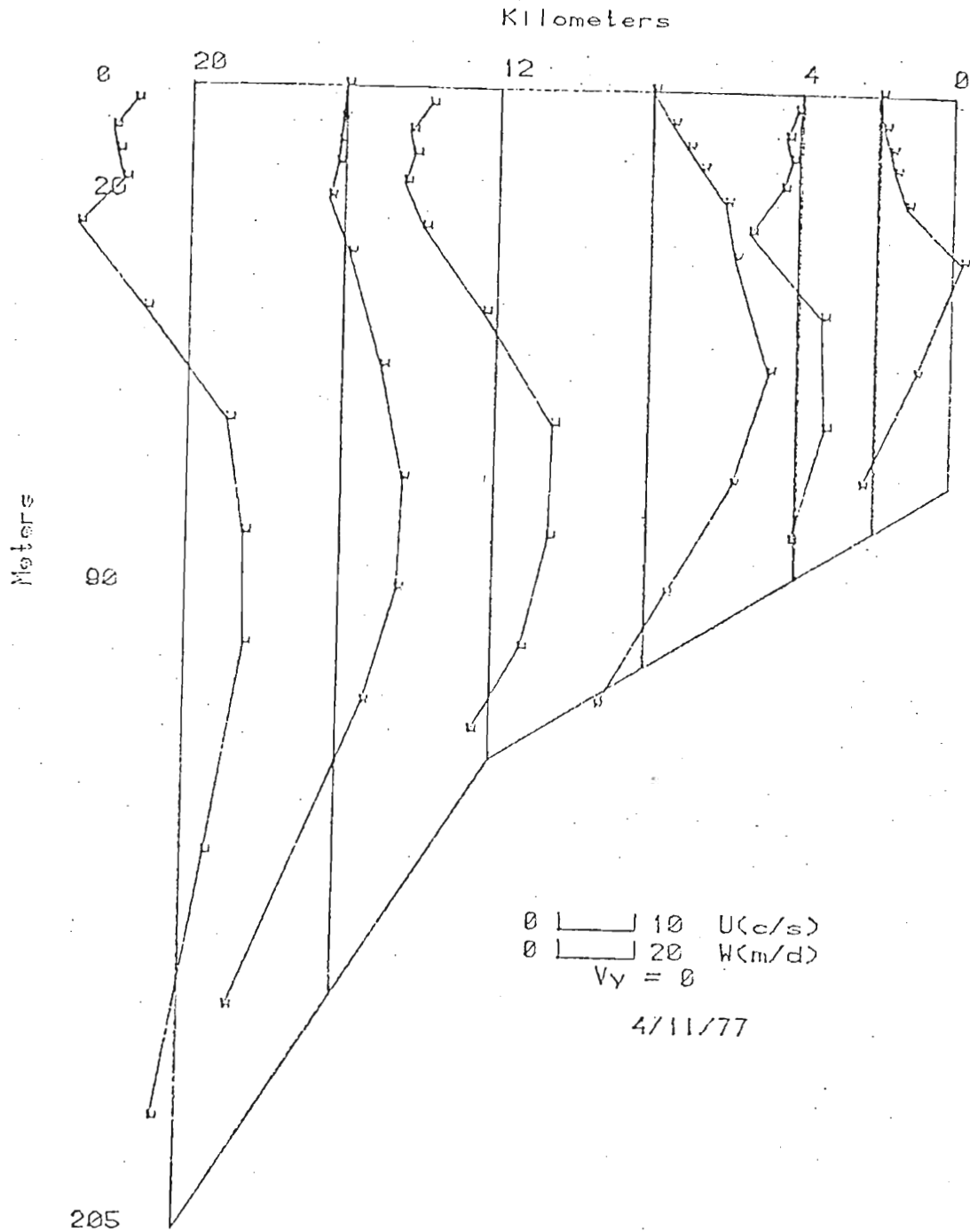
Fig. 18. Vertical cross shelf plot of adjusted u and w values obtained by O'Brien, Halpern and Smith (1979). Values to the left of the vertical reference line are negative and those to the right, positive.
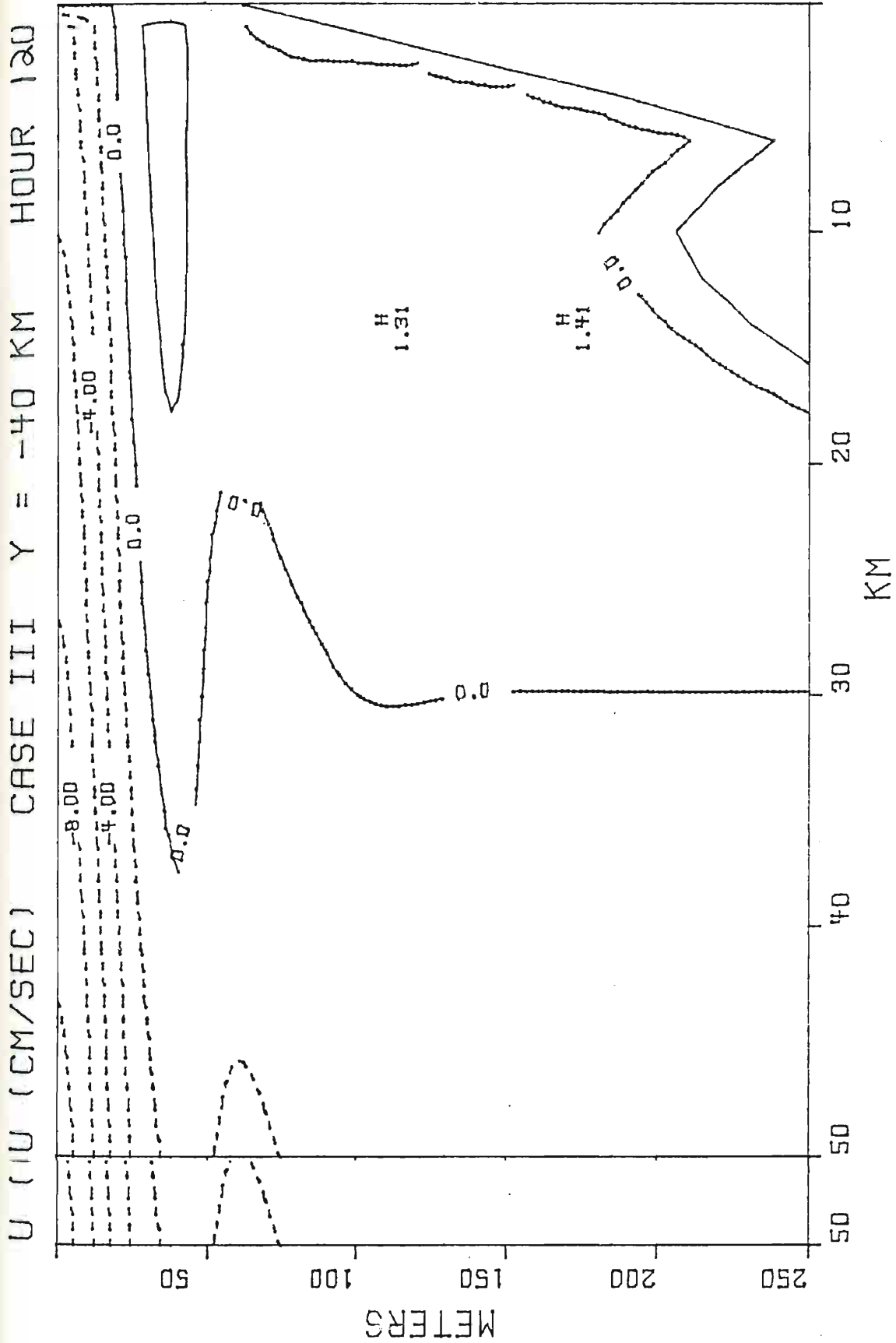
Fig. 19æig. 19a. Vertical cross section of the zonal velocity at day 5 obtained from model Case III. Values are ir are in cm s⁻¹. The y location of each figure may be obtained by looking at Fig: 5.
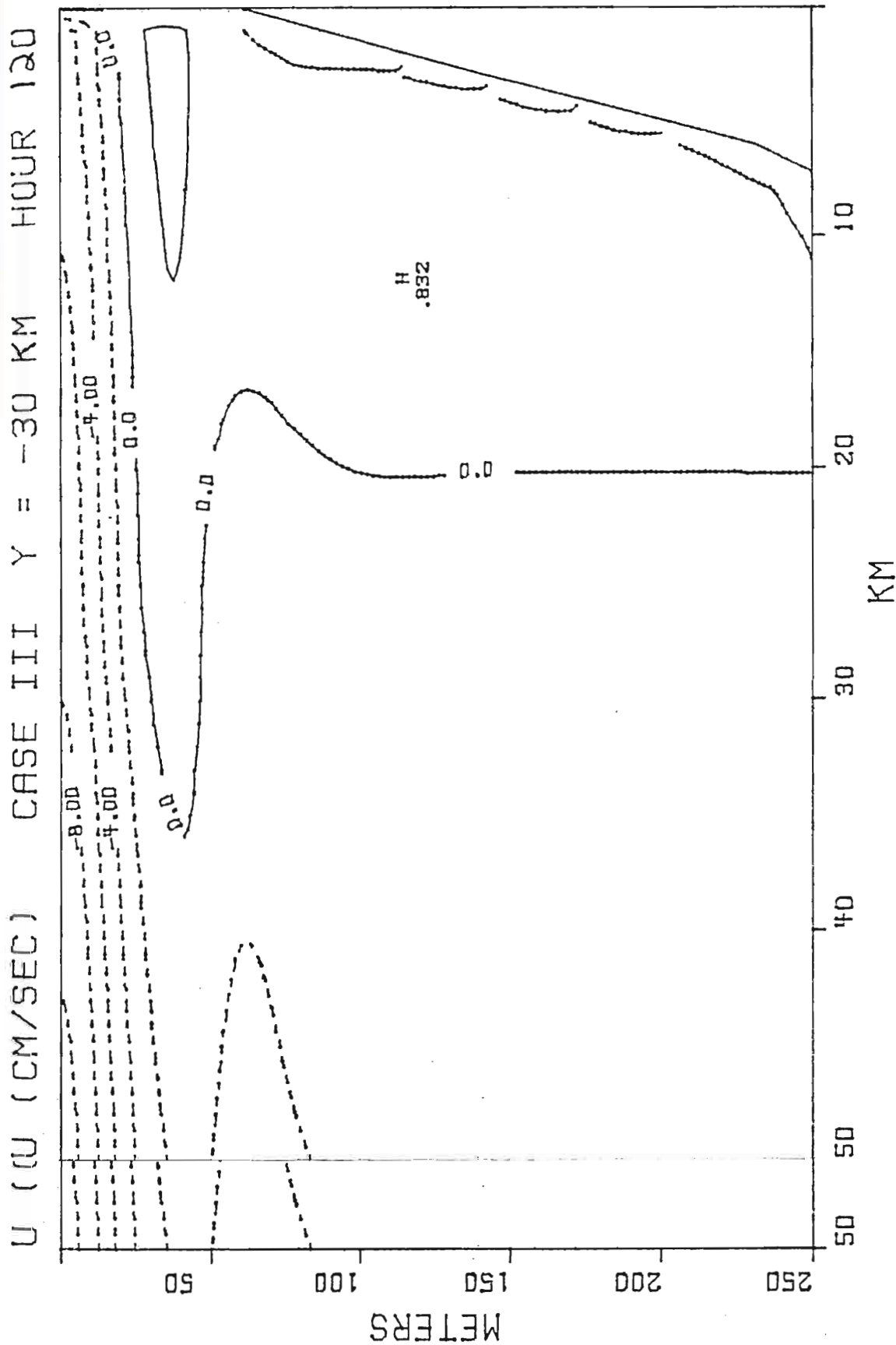
Fig. 19bg. 19b. Vertical cross section of the zonal velocity at day 5 obtained from model Case III. Values are in are in cm s^{-1}.
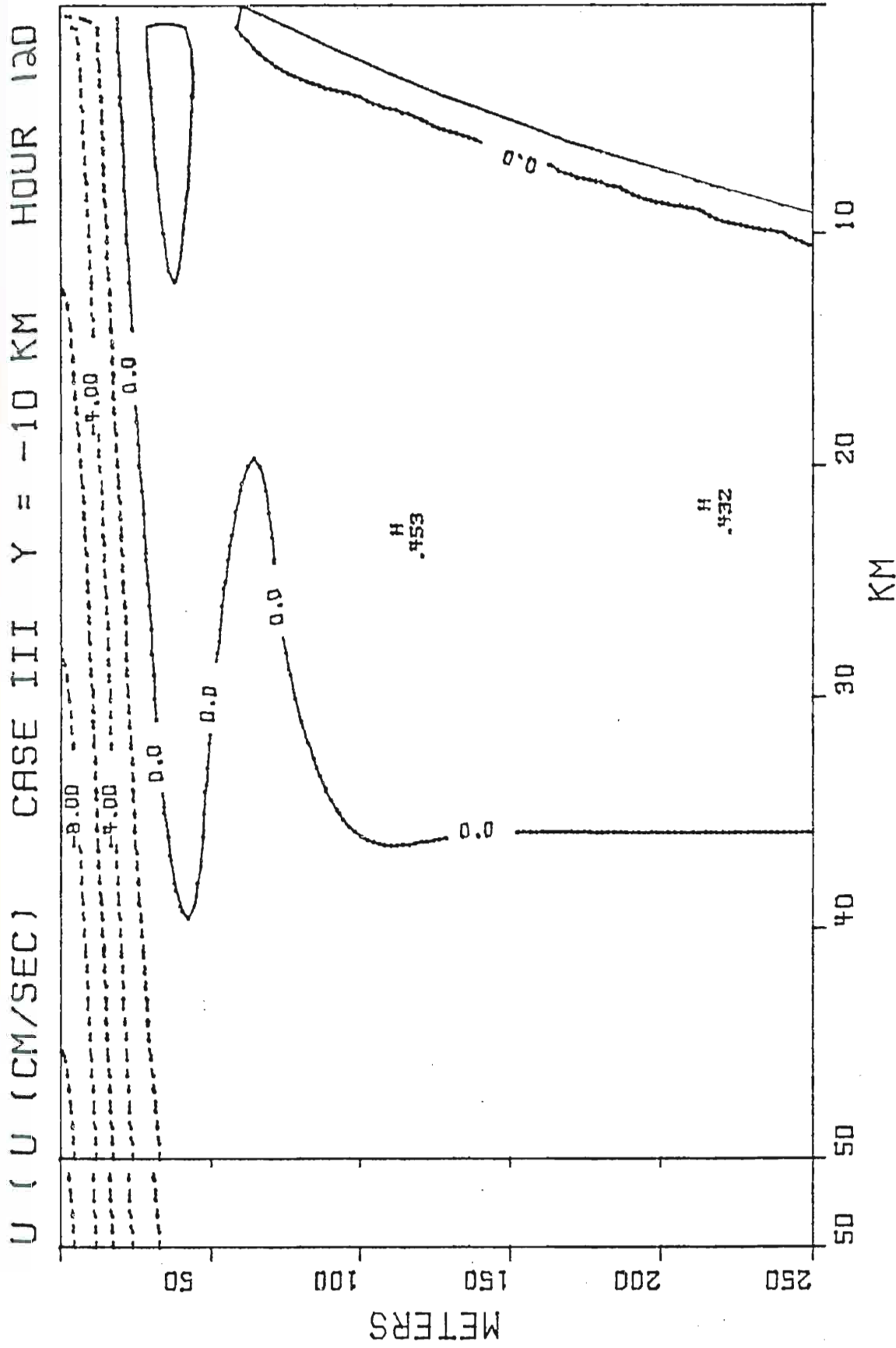
Fig. 19cig. 19c. Vertical cross section of the zonal velocity at day 5 obtained from model Case III. Values are in are in cm s^{-1}.

69
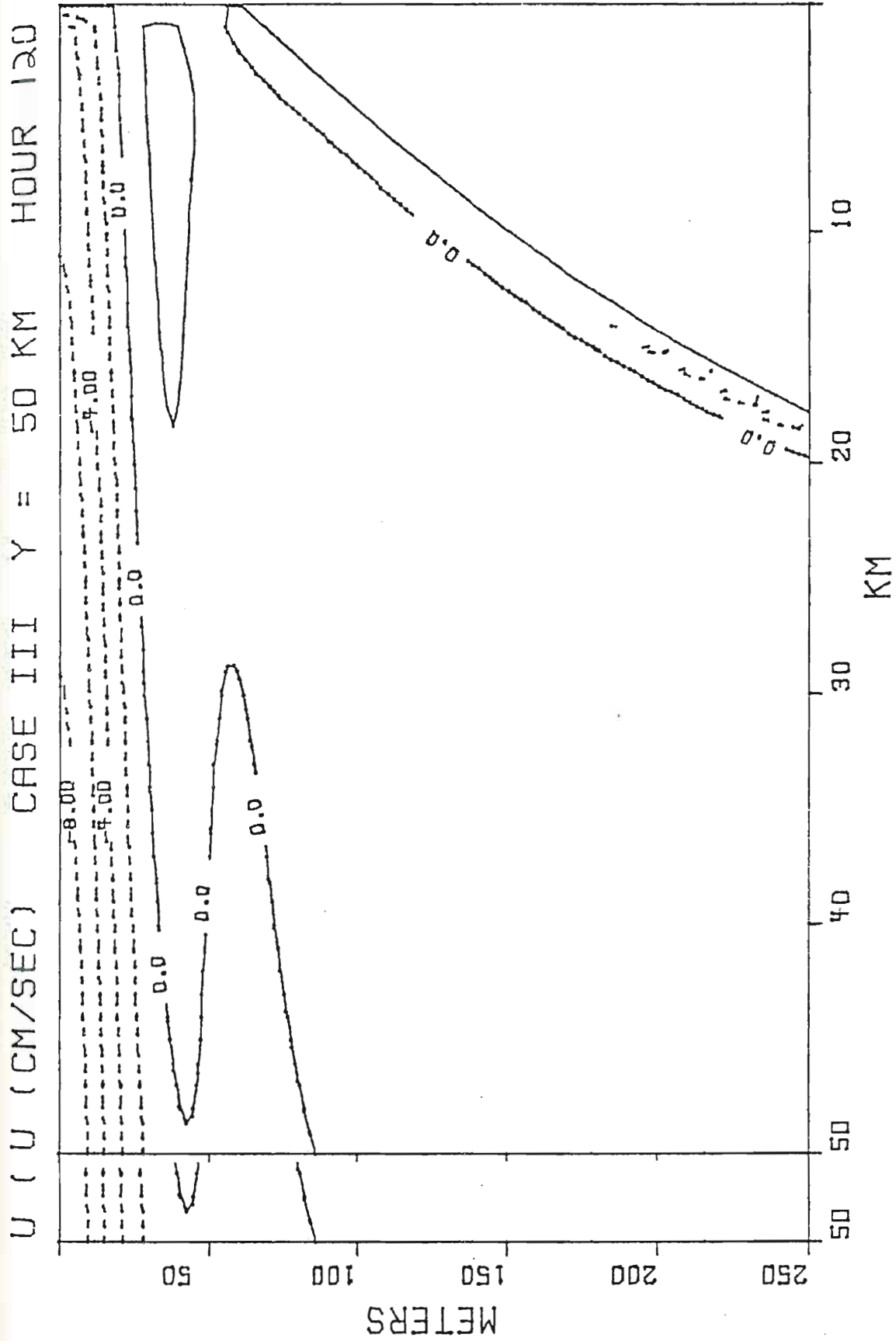
Fig. 19dig. 19d. Vertical cross section of the zonal velocity at day 5 obtained from model Case III.
Values are in are in cm s^{-1}.

becoming offshore. This onshore component combined with the total off-shore flow in the upper layer due to the wind stress, causes the narrow-ing of the offshore layer near the coast. An offshore flow dominates the remainder of the picture except for a narrow region above the shelf. As expected from previous results discussed, the onshore flow near the seamount is larger than over the broad shelf as seen in Fig. 21a. At $y = -30$ km, the region of sharp changes in topography just north of the seamount, the flow is seen to be onshore very near the coast, but becomes offshore at distances approximately 20 km offshore. This flow corresponds to the region between the two onshore maxima of Fig. 13a. Fig. 19c, at $y = -10$ km, is the approximate model location of the "C" Line for for JOINT II. In the first 20 km from the coast, an offshore flow of maximum value, 5 cm s^{-1}, is found in the upper 30 m. A weak flow, less than 2 cm s^{-1}, appears in a layer 16 m thick above the shelf. These layer thicknesses correspond closely to Van Leer's data. The magnitudes of the observed offshore flow is < 5 cm s^{-1} in both these layers, also close to the model values. The model onshore flow reaches a maximum of 2 cm s^{-1}, slightly less than Van Leer's 5 cm s^{-1}. Thus along the "C" Line, in both magnitude of the flow and thickness of the layer, the model values and observed values agree. Fig. 19d, rep-resents the cross sectional flow over the broad shelf in the northern portion of the basin. Features of the flow here differ little with the previous figure except in the thickness of the bottom offshore layer. The thickness of this layer, proportional to the inverse square root of the Coriolis parameter, is expected to increase approaching the equator.

the Coriolis parameter, is expected to increase approaching the equator.

5.   SUMMARY AND CONCLUSIONS

A two layer, x-y-t, β-plane numerical model, developed by Hurlburt (1974), has been used to investigate upwelling features off Peru. The model is nonlinear and neglects thermodynamics. Two idealized topographies have been incorporated into the model. One, a hyperbolic tangent representation of the topography, characterizes the broad shelf north of 15°S and narrow shelf south of 15°S. The second is an ellipse added to the hyperbolic tangent topography, simulating a mesoscale seamount. New to this model is the addition of an atmospheric pressure gradient as forcing along with the usual wind stress forcing.

Cases using the previously mentioned idealized topography and forcing functions were compared by viewing model results in the form of contour and vector plots. The first topography examined, revealed a maximum of upwelling over the broad shelf due to the effects of wind stress, a rising topography and mass continuity. With the addition of the seamount to the topography, a new upwelling maximum appeared just south of 15°S. This region has been documented by the JOINT II investigation as a region of large upwelling. Specifically, this study shows that this region of maximum upwelling is due to a mesoscale topographic feature, the seamount.

Topography is seen to affect the structure of both the upper layer and meridional velocity fields. The seamount appears to be the most

Topography is seen to affect the structure of both the upper layer and meridional velocity fields. The seamount appears to be the most

71

influential topographic feature. Its effects are apparent in both the
upper and the lower layer zonal flow. Topographic variations in the
lower layer longshore flow result in variations in the barotropic zonal
flow. The scale of the effects of the topography on these flows is
larger than that of the topography itself.

In general, the patterns of meridional and zonal velocity result-
ing from the model are in good agreement with observation. The verti-
cal cross sections reveal on offshore upper layer of increasing thick-
ness, an onshore layer below and another offshore flow near the bottom
due to Ekman dynamics. The magnitude of the flow fields are also in
good agreement with observation. The zonal velocity has been shown to
be approximately equal to that observed. The meridional flow seems to
be generally larger than the observed flow. A reduction in the value
chosen for the pressure gradient will reduce the magnitude of these
flows.

The method described in Hurlburt (1974) and Peffley and O'Brien
(1976), that is, use of a wind-driven system, does not serve to cor-
rectly model the observed upwelling system off Peru. Wind stress for-
cing alone produced no poleward flow. The reason for this apparently
lies in the 45° rotation of the model. This rotation reduced the β
effect enough so that a sufficiently large N-S pressure gradient, cap-
able of reducing the barotropic mode and allowing the development of
a poleward flow, is not induced. Thus another mechanism responsible
for the poleward flow must be found. Atmospheric pressure gradient
forcing was chosen to serve this purpose. Including atmospheric pres-
forcing was chosen to serve this purpose. Including atmospheric pres-
sure gradient forcing along with the wind stress forcing has been
shown to not only induce a lower layer poleward flow, but also induce

flow patterns that agree with observation in both layers. With the addition of this mechanism, the model is able to correctly predict the location of the areas of maximum upwelling.

In summary, it must be remembered that this model is an idealized model designed to explain the dynamics of upwelling off Peru. Due to a constant forcing by wind stress and the atmospheric pressure gradient, this model results in somewhat steady flows. Studies of the time-varying forcing should provide more realistic solutions. The exclusion of thermodynamics, which allows only five days of useful integration, should also be reconsidered when designing a more realistic model. A more detailed study of the instabilities caused by very large isobathic gradients may allow for the use of a smaller horizontal eddy viscosity. Finally, improvement on the solutions at the northern and southern boundaries could be made.

It may be concluded then, that the choice of the atmospheric pressure gradient as an additional means of forcing to the Hurlburt (1974) model, serves to correctly simulate the flows seen off the coast of Peru. It is also concluded that the two upwelling maxima observed are due to topographic effects, in particular the maximum observed south of of 15°S is a result of the seamount, a mesoscale topographic feature.

APPENDIX I

List of Symbols

A	horizontal coefficient of eddy viscosity
A_v	vertical coefficient of eddy viscosity
C_I, C_B	drag coefficients for interfacial and bottom friction
$D(x, y)$	height of the bottom topography above a reference level
f	Coriolis parameter
f_o	Coriolis parameter at $y \simeq 0$
g	acceleration of gravity
g'	reduced gravity defined as $\dfrac{g(\rho_2 - \rho_1)}{\rho_2}$
h	total depth
h_1, h_2	instantaneous local layer thicknesses
H_1, H_1	initial layer thicknesses
L_x, L_y	the dimensions of model in the x and y directions
t	time
u_1, u_2	x-directed components of current velocity
v_1, v_2	y-directed components of current velocity
x, y, z	Cartesian coordinates for a 45° rotated system; x is positive north eastward, y is positive north westward, and z is positive upward
β	$\dfrac{\partial f}{\partial y}$, $\dfrac{\partial f}{\partial x}$
β_{Ty}	value of β simulated by a N-S sloping topography
β	value of β simulated by a E-W sloping topography
β_{Ty}	value of β simulated by a N-S sloping topography
β_{Tx}	value of β simulated by a E-W sloping topography

74

Δt	time increment in the numerical integration
Δx, Δy	horizontal grid increment in x and y
ρ, ρ_1, ρ_2	densities of sea water
σ_t	$(\rho_s, t, o - 1) \times 10^3$ where ρ_s, t, o is the sea water density corrected to atmospheric pressure
τ_{sx} τ_{Ix} τ_{Bx}	x directed tangential stresses at the surface, interface and bottom
τ_{sy} τ_{Iy} τ_{By}	y directed tangential stress at the surface, interface and bottom

APPENDIX B

CROSS SHELF PHYSICS SYSTEM OF EQUATIONS

The problem discussed in section 2c was

$$\frac{\partial^2 w_1}{\partial z^2} - s^2 w_1 = 0 \qquad\qquad b \leq z \leq 0$$

and

$$\frac{\partial^2 w_2}{\partial z^2} - s^2 w_2 = 0 \qquad\qquad c \leq z \leq b$$

where $z = 0$ is the sea surface, $z = b$ is the pynocline and $z = c$ is the bottom and

$$w_1 = u_1' + iv_1'$$
$$w_2 = u_2' + iv_2'$$

The problem requires the integral constraints

$$\int_b^0 w_1 \, dz = \int_c^b w_2 \, dz = 0$$

and the boundary conditions

$$\frac{\partial w_1}{\partial z} = \frac{\tau_{sy}}{A_v} + i \frac{\tau_{sy}}{A_v} = P \qquad\qquad z = 0$$

$$w_2 = w_1 + \Delta v = J \qquad\qquad z = b$$

$$w_2 = w_1 + \Delta v = J \qquad\qquad z = b$$

$$\frac{\partial w_1}{\partial z} = \frac{\partial w_2}{\partial z} \qquad\qquad z = b$$

$$w_2 = - (u_2 + iv_2) = K \qquad\qquad z = c$$

A_v refers to the vertical eddy viscosity. The components of the surface wind stress in the x and y directions are τ_{sx} and τ_{sy}. Also

$$r = (\frac{f}{2A_v})^{1/2}$$

$$s = (1 + i)r$$

$$\Delta v = u_1 - u_2 + i(v_1 - v_2)$$

The solution to this system of equations after Thompson (1974) yield, for the upper layer,

$$w_1 = \frac{A_1 e^{sz}}{s} - \frac{B_1 e^{-sz}}{s} + C_1$$

where

$$A_1 = P - B_1$$

$$B_1 = Pe^{sb} - Q$$

$$C_1 = \frac{1}{b} [\frac{A_1}{s^2} (1 - e^{sb}) + \frac{B_1}{s^2} (1 - e^{-sb})]$$

and

$$Q = \frac{Y - \varepsilon R - \varepsilon \Delta v}{1 + \varepsilon \eta}$$

$$Y = X + \frac{[\mu s K \gamma_1 \gamma_3 + \mu s \alpha_1 K]}{\alpha_1 \gamma_2 - \alpha_2 \gamma_1}$$

$$\varepsilon = \frac{\mu s \alpha_1}{\underline{\quad\quad\quad}}$$

$$\varepsilon = \frac{\mu s \alpha_1}{\alpha_1 \gamma_2 - \alpha_2 \gamma_1}$$

$$\mu = \frac{\alpha_2}{\alpha_1} e^{sb} + e^{-sb}$$

$$X = \frac{K \gamma_3 s e^{sb}}{\alpha_1}$$

$$\alpha_1 = e^{sc} \gamma_3 - \frac{\gamma_1}{s}$$

$$\alpha_2 = e^{-sc} \gamma_3 + \frac{\gamma_2}{s}$$

$$\alpha_3 = - \frac{(\gamma_3)^2}{2}$$

$$\gamma_1 = e^{sb} - e^{sc}$$

$$\gamma_2 = e^{-sb} - e^{-sc}$$

and

$$\gamma_3 = b-c \quad .$$

In the lower region

$$w_2 = \frac{A_2 e^{sz}}{s} - \frac{B_2 e^{-sz}}{s} + C_2$$

where

$$A_2 = [K \gamma_3] \frac{s}{\alpha_1} + \frac{B_2 \alpha_2}{\alpha_1}$$

$$B_2 = s \left[\frac{K\gamma_1\gamma_3 - \alpha_1 (J - K + \Delta v)}{\alpha_1 \gamma_2 - \alpha_2 \gamma_1} \right]$$

$$C_2 = K - \frac{A_2 e^{sc}}{s} + \frac{B_2 e^{-sc}}{s}$$

$$C_2 = K - \frac{A_2 e^{sc}}{s} + \frac{B_2 e^{-sc}}{s}$$

and

$$J = R + \frac{(Y - \varepsilon R - \varepsilon \Delta v)}{1 + \varepsilon \eta}$$

$$\eta = \frac{1}{s} [\coth(sb) - \frac{1}{sb}]$$

$$\delta_1 = e^{sb} (1 - \coth(sb)) + \frac{1}{sb}$$

$$\delta_2 = \coth(sb) - \frac{1}{sb}$$

$$\delta_3 = \frac{e^{sb}}{s} (1 - \coth(sb)) + \frac{\coth(sb)}{s} - \frac{b}{2} .$$

REFERENCES

Allen, J.S., 1973: Upwelling and coastal jets in a continuously strat-
ified ocean. J. Phys. Oceanogr., 3, 245-257.

Barton, E.D., 1977: JOINT II - RIV Thomas G. Thompson Cruise 108 Leg I
CTD Measurements off the coast of Peru near Cabo Nazca April - May
1976. CUEA data report 39.

Brink, K. H., J.S. Allen and R.L. Smith, 1978: A study of low frequen-
cy fluctuations near the Peru coast. J. Geophys. Res., in press.

Crank, J., and P. Nicholson, 1947: A practical method for numerical
evaluation of solutions of partial differential equations of heat
conduction type. Proc. Camb. Phil. Soc., 43, 50-67.

Garvine, R.W., 1971: A simple model of coastal upwelling dynamics. J.
Phys. Oceanogr., 1, 169-179.

Grammeltvedt, A., 1969: A survey of fine-difference schemes for the
primitive equations for a barotropic fluid. Mon. Wea. Rev., 97,
384-404.

Hsueh, Y., and J.J. O'Brien, 1971: Steady coastal upwelling induced by
an along-shore current. J. Phys. Oceanogr., 1, 180-186.

Hurlburt, H.E., 1974: The influence of coastline geometry and bottom
topography on the eastern ocean circulation. Ph.D. Thesis, Florida
State University, 103 pp.

_____, and J. Dana Thompson, 1973: Coastal upwelling on a β-plane.
J. Phys. Oceanogr., 3, 16-32.

Kullenberg, G., 1971: Vertical diffusion in shallow waters. Tellus,
23, 129-135.

Mittelstaedt, E., 1978: Physical oceanography of coastal upwelling re-
gions with special reference to Northwest Africa. Symposium on
the Canary Current: Upwelling and Living Resources No. 40, part
ii.

O'Brien, J.J. and H.E. Hurlburt, 1972: A numerical model of coastal
upwelling. J. Phys. Oceanogr. 2 14-26.
ii.

O'Brien, J.J. and H.E. Hurlburt, 1972: A numerical model of coastal
upwelling. J. Phys. Oceanogr., 2, 14-26.

_____, D. Halpern and R.L. Smith, 1979: Determination of vertical velocity on the continental shelf. To be submitted to J. Phys. Oceanogr.

Peffley, M.B., and J.J. O'Brien, 1976: A three dimensional simulation of coastal upwelling off Oregon. J. Phys. Oceanogr., 6, 164-180.

Preller, R.H., 1977: Peru near shore bathymetry map and contoured bottom topography map. CUEA Newsletter, 6, No. 4, 48-50.

Proudman, J., 1953: Dynamical Oceanography. London, Metheun, 409 pp.

Schulman, E.E., 1970: The antarctic circumpolar current. Proc. of the 1970 Summer Computer Simulation Conference, Denver, Colorado, 955-968.

Smith, R.L., 1978a: Physical Oceanography of Coastal Upwelling Regions. A comparison: Northwest Africa, Oregon and Peru. Symposium on the Canary Current: Upwelling and Living Resources No. 40.

_____, 1978b: Poleward propagating perturbations in currents and sea level along the Peru coast. J. Geophys. Res., in press.

_____, D.B. Enfield, T.S. Hopkins and R.D. Pillsbury, 1971: The circulation in an upwelling ecosystem: the Pisco cruise. Inv. Pesq., 35: 9-24.

Stevenson, M.R., R.W. Garvine, and B. Wyatt, 1973: Lagrangian measurements in the coastal upwelling zone off Oregon. J. Phys. Oceanogr., 4, 321-336.

Stuart, D.W. and M. Nanney, 1978: Maps of mean sea surface temperatures during JOINT II 1976 and 1977. CUEA Synapse Notes No. 4, 2.

Thompson, J.D., 1974: The coastal upwelling cycle on a beta plane: Hydrodynamics and thermodynamics. Ph.D. Thesis, Florida State University, 141 pp.

_____, and J.J. O'Brien, 1973: Time dependent coastal upwelling. J. Phys. Oceanogr., 3, 33-46.

Tomczak, M., 1970: Schwankungen von Schichtung und Stromung in westafricanischen Auftriebsgebiet wahrend der Deutchen Nordatlantichen Expedition 1973. An excerpt from "Meteor" Forschungsergebrisse Reihe A, Heft 7. Gebruder Borntraeger, Berlin, pp. 1-109.

Van Leer, J.C., 1979: Cyclosonde data. To appear in a CUEA data report, February, 1979.

Van Leer, J.C., 1979: Cyclosonde data. To appear in a CUEA data report, February, 1979.